Eur. Phys. J. C (2025) 85:1008
https://doi.org/10.1140/epjc/s10052-025-14717-6

THE EUROPEAN PHYSICAL JOURNAL C

Regular Article - Theoretical Physics

Observational constraints and cosmological evolution in Finsler Barthel–Kropina space-time

J. Praveen[1,a], **S. K. Narasimhamurthy**[1,b], **Rajesh Kumar**[2,c]

[1] Department of P.G. Studies and Research in Mathematics, Kuvempu University, Shankaraghatta, Shivamogga, Karnataka 577451, India
[2] Department of Mathematics and Statistics, Deen Dayal Upadhyaya Gorakhpur University, Gorakhpur, U.P., India

Received: 3 May 2025 / Accepted: 30 August 2025

Abstract Finslerian gravity provides a compelling extension to standard cosmology by allowing for direction-dependent effects in the structure of space-time. In this study we analyze the cosmological evolution of a modified FLRW universe with an anisotropic parameter modeled with a linear redshift dependence within the Barthel–Kropina Finsler framework. We consider two models for dark energy: Model-1, which assumes a constant dark energy equation of state parameter ($\omega_{\rm de}$=constant) and Model-2, which adopts a redshift-evolving CPL form $\omega_{\rm de}(z)=\omega_0+\omega_1\frac{z}{1+z}$. Using observational data from cosmic chronometers (CC), baryon acoustic oscillations (BAO) and Pantheon + Supernovae we perform parameter estimation with Markov Chain Monte Carlo techniques and analyze cosmographic quantities. Our analysis of the deceleration parameter confirms the presence of late-time cosmic acceleration, consistent with observations. Both Finslerian models yield statistical fits to the data that are comparable to those of the standard ΛCDM cosmology. Model-1 yields statistical results comparable to those of ΛCDM in both AIC and BIC analyses. Model-2, with its evolving dark energy equation of state allows for a more flexible description of late-time cosmic acceleration. Under current observational constraints both models describes the late-time anisotropy and offer a framework to explore deviations from cosmic isotropy beyond the standard cosmological constant scenario.

Contents

[a] e-mail: praveenjayarama1998@gmail.com
[b] e-mail: sknmurthy@kuvempu.ac.in
[c] e-mail: rajesh.mathstat@ddugu.ac.in (corresponding author)

Published online: 17 September 2025

1 Introduction

The discovery of the universe's accelerating expansion marked a pivotal shift in cosmology, overturning the long-held expectation that gravitational attraction would gradually decelerate cosmic expansion. Observations of distant Type Ia supernovae (SN Ia) revealed an unexpected dimming, interpreted as evidence for acceleration, which implied the presence of a previously unknown component now termed dark energy. Subsequent confirmations from cosmic microwave background (CMB) measurements and large-scale structure surveys established this accelerated expansion as a cornerstone of the standard cosmological model. Currently, dark energy is understood to comprise approximately 70% of the total energy density of the universe, playing a dominant role in its present dynamics and suggesting a future of perpetual expansion with profound implications for the ultimate fate of the cosmos [1–10]. One of the simplest interpretations involves a small positive cosmological constant Λ supported by SN Ia observations and addressed within the broader context of the cosmological constant problem. This has motivated future missions, such as Planck, aimed at refining key cosmological parameters [11,12]. Alternative accelerating models, including phantom energy with an equation of state parameter, $\omega < -1$ have also been explored and show strong agreement with observational data [13,14]. Recent studies emphasize the importance of a redshift-dependent equation of state for dark energy, which enables more dynamic modeling and better fits to combined datasets [15–18].

While these approaches have advanced our understanding of cosmic acceleration models and dark energy, they primarily rely on the Riemannian geometric framework and assume fundamental homogeneity and isotropy. Ongoing theoretical challenges and observed anomalies have motivated the investigation of more general geometric structures, especially those incorporating anisotropy (see [19] and references therein). Finsler geometry has been applied to Einstein vacuum field equations, resulting in a modified Birkhoff theorem and the development of locally anisotropic space-time models that extend gravitational theory [20,21]. Further studies have explored Lorentz invariance violations and generalized Lorentz transformations in Finslerian spaces [22], as well as the integration of Kaluza–Klein, Finsler, and Lagrange geometries in constructing anisotropic super-string models [23,24]. Anisotropy vectors have provided new frameworks for analyzing CMB anisotropies in agreement with Planck data, while the inclusion of anisotropic fields and fluids in cosmological models has refined our understanding of cosmic evolution [19,25,26]. Recent work underscores the potential of Finsler geometry to address galactic rotation anomalies and enhance cosmological modeling [27].

Recent developments in Finslerian cosmology have demonstrated that modifications to the standard FLRW model, particularly through the use of curved Finslerian space-time and general very special relativity (VSR) can offer alternatives to dark energy for explaining the observed acceleration of the universe [28,29]. These frameworks support the exploration of Lorentz-violating theories, potential quantum gravity corrections and the investigation of photon time delays in high-energy astrophysical phenomena such as gamma-ray bursts [30,31]. Finsler gravity has also been shown to provide a flexible extension of general relativity capable of addressing cosmological anisotropies, late-time cosmic acceleration, and departures from isotropy [32]. Metrics such as Finsler–Randers and Finsler–Kropina have enabled the formulation of generalized Friedmann equations and stable cosmological solutions, opening up new avenues for probing the fundamental geometry of space-time [33]. These advances have further facilitated the development of cosmological models featuring enriched geometric structures, scalar-tensor theories for dark energy and inflation, and new theoretical effects that may be testable with observations, thus extending the possibilities beyond the standard ΛCDM paradigm [34–42].

Building on recent advances in Finsler gravity, the current study develops a cosmological framework within the Barthel-Kropina geometric setting, offering a distinct approach to modeling anisotropic space-time. By employing Barthel connection, the formalism naturally integrates direction-dependent anisotropies into the cosmological background, providing an alternative to conventional isotropic models. We introduce a redshift-dependent parameterization $\eta(z)$ to dynamically track anisotropic effects throughout cosmic evolution. Through a comprehensive observational analysis using Markov Chain Monte Carlo (MCMC) techniques and current CC, BAO, and Pantheon+ Supernovae data we deliver new constraints on the Barthel–Kropina model parameters.

The paper is organized as follows: the Sect. 2 introduces fundamental concepts of Finsler geometry related to Kropina and Barthel connections. Section 3, where we derive the Finsler-Barthel-Kropina metric and discuss the gravitational field equations in this background. Section 4 describes the details of observational datasets and the methodology employed, including MCMC analysis and χ^2-statistic, to constrain the model parameters. Section-5 introduces the parametrization of the anisotropic factor $\eta(z)$ and the equation of state $\omega(z)$ of dark energy to analyze the cosmological evolution. Section 6 discusses the parameter estimation for Model-1 and Model-2 through CC, BAO, and SNe Ia observational data. Section 6.3 explores the observational and theoretical comparisons of the Hubble function and distance magnitude. Physical viability of the models and Cosmographic parameters for both models are discussed in Sect. 7 and *Om(z)* diagnostic analysis of the models is also studied and Sect. 8 presents the model selection analysis employing information criteria to quantitatively compare the statistical performance of the proposed cosmological models. The last

Sect. 9 provides the summary and the future perspectives of the work.

2 Overview of Finsler geometry and connections

2.1 Finsler metric structure

The Finsler geometry extends Riemannian geometry by defining distances in a way that depends not only on the magnitude of displacement between points (coordinate) but also on its direction. Unlike Riemannian geometry, where the distance between two points is simply the length of the shortest curve connecting them, Finsler geometry uses a metric that accounts for both the direction and magnitude of the displacement vector. This broader definition allows Finsler geometry to describe spaces with asymmetric or anisotropic properties [43–46].

In Finsler spaces, the infinitesimal interval ds between two nearby points x^i and $x^i + dx^i$ is given by $ds = F(x^i, dx^i)$, where F is the Finsler metric function, defined on a smooth manifold M by $F : TM \to \mathbb{R}$ and satisfies the following properties [43]:

- F is C^∞ on $\tilde{TM} = TM\backslash\{0\}$ and continuous on the null section of the projection $\pi : TM \to M$.
- F is positively homogeneous of degree one with respect to the fiber coordinates, meaning $F(x, ky) = kF(x, y)$ for any $k > 0$.
- For any point $(x, y) \in \tilde{TM}$, the symmetric bilinear form $\hat{g}_{ij}(x, y)$ is non-degenerate and has a constant signature, where

$$\hat{g}_{ij}(x, y) = \frac{1}{2}\frac{\partial^2 F^2(x, y)}{\partial y^i \partial y^j}. \tag{1}$$

Here, (x^i, y^j) are the canonical coordinates on the tangent bundle, and $y = y^i \frac{\partial}{\partial x^i}$ represents a tangent vector at $x \in M$. The line element is expressed as

$$ds^2 = F^2(x^i, y^i) = \hat{g}_{ij}(x^i, y^i) y^i y^j. \tag{2}$$

Using the homogeneity property of F, the Eq. (1) can also be rewritten as

$$\hat{g}_{ij}(x, y) y^i y^j = F^2. \tag{3}$$

The Eq. (2) then becomes

$$ds^2 = \hat{g}_{ij}(x, y) y^i y^j. \tag{4}$$

The Eq. (4) now describes the line element in Finsler spaces, where the metric tensor $\hat{g}_{ij}$ varies based on both direction and magnitude.

The case when $\hat{g}_{ij}(x, y) = \hat{g}_{ij}(x)$ conforms to that of a Riemannian space, reliant only on position coordinate which is also characterized by the vanishing of the Cartan tensor C_{ijk}

$$\hat{C}_{ijk} = \frac{\partial \hat{g}_{ij}(x, y)}{\partial y^k} = \frac{1}{4}\frac{\partial^3 F^2}{\partial y^i \partial y^j \partial y^k} = 0. \tag{5}$$

The osculating Riemannian approach simplifies computations in Finsler geometry by approximating a Finsler structure with a Riemannian one which is obtained by evaluating the Finsler metric $\hat{g}_{ij}(x, y)$ along a non-zero vector field $Y(x)$, yielding the osculating metric $\hat{g}_{ij}(x) = \hat{g}_{ij}(x, Y(x))$. The osculating method bridges this gap by projecting geometric quantities from TM to M, enabling the use of familiar Riemannian tools for analyzing Finslerian structures [1,3].

2.2 Barthel connection

The Barthel connection is introduced to address the limitations of the Berwald connection while simplifying some aspects of the Cartan connection [46–50]. Suppose we introduce a specific structure $(M, F(x, y), Y(x))$ representing a Finsler space $(M, F(x, y))$ having a non-zero tangent vector field $Y(x)$ defined on M. If Y is nowhere vanishing, the Finslerian metric gives rise to Y-Riemannian metric. The Y-tensor field associated with the fundamental tensor $\big(g_{ij}(x, Y(x))\big)$ is called Y-Riemannian metric structure. The Barthel connection is metric compatible with respect to the Y-Riemannian metric and also has the torsion tensor. This metricity ensures that the length of vectors is preserved under parallel transport, which aligns better with physical intuitions and makes the connection more suitable for studying physical systems. The Barthel connection treats Finsler spaces as the point Finsler spaces and is locally Minkowskian and in general, it is not locally Euclidean. For a Finsler space, the linear Barthel-connection associated to the Cartan connection is the Levi–Civita connection of the Y-Riemannian space. Thus, Barthel connection corresponds to the linear Y-Connection associated with the Cartan connection through a nonzero tangent vector field $Y(x)$.

Then, the differential of the vector field $Y^i(x)$ with respect to the Barthel connection is defined as [46,49,50]

$$DY^i = dy^i + Y^k b^i_{kh}(x, Y) dx^h, \tag{6}$$

where, b^i_{kh} is Barthel connection coefficient defined by using generalized Christoffel symbols which are given by

$$\gamma_{ijk}(x, y) = \frac{1}{2}\left[\frac{\partial g_{jk}}{\partial x^i} + \frac{\partial g_{ki}}{\partial x^j} - \frac{\partial g_{ij}}{\partial x^k}\right]. \tag{7}$$

and the Barthel connection coefficients in equation (6) are defined as [40,41,47–49]

$$b^i_{kh} = \gamma^i_{kh} - \gamma^r_{ks} Y^s C^i_{rh}, \tag{8}$$

where, C^i_{jk} is the Cartan torsion tensor. The Barthel connection is the simplest connection, which upholds the metric

function by parallel transport, making it a metric-compatible connection.

Barthel connection has the specific properties are that the Y-linear connection associated to the Cartan Y-linear connection and metrical with respect to the Y-Riemannian metric and has the torsion

$$\mathcal{T}^i_{jk} = C^i_{jr}(x, Y(x))Y^r_k - C^i_{kr}(x, Y(x))Y^r_j \tag{9}$$

which is non-zero in the Finsler space. Specifically, it ensures that the metric function remains invariant during such transport. Barthel connection depends on the field to which it is applied and it depends only on the direction of the field to which it is applied and it preserves parallel transport.

In the Y-Riemannian region, the curvature tensor $R^i{}_{jkl}$ associated with the Barthel connection, corresponding to a vector field $Y(x)$, is referred to as the Y-*curvature tensor* and is given by

$$R^i_{jkl} = -\frac{\partial b^i_{jk}}{\partial x^l} + \frac{\partial b^i_{jl}}{\partial x^k} + \left(\frac{\partial b^i_{jk}}{\partial Y^s} b^s_{pl} - \frac{\partial b^i_{jl}}{\partial Y^s} b^s_{pk}\right) Y^p + b^i_{rk} b^r_{jl} - b^i_{rl} b^r_{jk}. \tag{10}$$

This curvature property applies to both space and points and the curvature is evaluated solely based on the direction of the field. Subsequently, by contracting the point curvature we obtain the Ricci tensor denoted as $R_{jk} = R^i_{jki}$, and the Ricci scalar $R = R^i_i$.

2.3 The osculating-Riemannian space approach

Unlike Riemannian geometry, where connections live on a manifold of the manifold, the Finslerian connections live on the total space of the tangent bundle. To facilitate the derivation and comparison of different covariant derivatives, the technique of the osculating Riemannian space approach can be employed [44,46]. This distinction gives rise to a fundamental geometrical contrast between the theories of Riemannian and Finsler manifolds. Thus, to overcome these dissimilarities, we can introduce the non-vanishing vector field Y on the manifold and obtain the $\mathcal{Y}$-Riemannian metric on the manifold. This methodology streamlines the computation of connection coefficients within Finsler space. The notion of osculation entails the transformation of the intricate characteristics of a Finsler structure and its associated connections into simpler structures. Specifically, these simpler structures involve components such as the Riemannian metric, affine connections or linear connections. This approach results in simplifying the complexities inherent in Finsler geometry and its connections. The methodology involved in this technique is outlines as below:

To construct an osculating Riemannian metric, consider a local section U of the projection $\pi_M : TM \to M$. By evaluating the Finslerian metric $g_{ij}(x, y)$ along the vector field $\mathcal{Y}(x) \neq 0$, the osculating Riemannian metric is defined as

$$g_{ij}(x) = g_{ij}(x, y)\big|_{y=Y(x)}, \quad x \in U, \tag{11}$$

where, U is a region on M. This particular region $(U, \mathcal{Y}(x))$ is termed the osculating Riemannian manifold along the curve C. Within this region U, it becomes feasible to employ the conventional covariant derivative derived from Riemannian geometry [44,46]. This derivative arises from the parallelism of Levi–Civita and the concept of osculation. Thus, the differential geometry of a curve C in a Finsler space can be studied using the corresponding osculating Riemannian space. This approach simplifies the determination of connection coefficients such as those for the Rund and Barthel connections. The pair (U, g_{ij}) forms a Riemannian manifold, with $g_{ij}(x)$ referred to as the $\mathcal{Y}$-osculating Riemannian metric.

Then the Christoffel symbols corresponding to this metric are given by

$$\gamma_{ijk}(x) = \frac{1}{2}\left(\frac{\partial g_{ik}(x, y(x))}{\partial x^j} + \frac{\partial g_{ij}(x, y(x))}{\partial x^k} - \frac{\partial g_{jk}(x, y(x))}{\partial x^i}\right). \tag{12}$$

2.4 Geodesic equations within the osculating Riemannian framework

In Finsler geometry, geodesics follow from the Euler–Lagrange equations for the fundamental function given by

$$\frac{d}{dt}\left(\frac{\partial F(x, y)}{\partial y^i}\right) - \frac{\partial F(x, y)}{\partial x^i} = 0, \tag{13}$$

This yields the Finslerian geodesic form

$$\frac{d^2x^i}{ds^2} + \gamma^i{}_{jk}(x, y)\, y^j y^k = 0, \tag{14}$$

where the Finslerian Christoffel symbols $\gamma^i{}_{jk}(x, y)$ are defined by the metric

$$\gamma_{ijk}(x, y) = \frac{1}{2}\left(\frac{\partial g_{ik}(x, y)}{\partial x^j} + \frac{\partial g_{ij(x,y)}}{\partial x^k} - \frac{\partial g_{jk}(x, y)}{\partial x^i}\right), \tag{15}$$

and $\gamma^i{}_{jk} = g^{i\ell}\gamma_{\ell jk}$. Using the chain rule one obtains

$$\gamma^i{}_{jk}(x) = \gamma^i{}_{jk}(x, y)\big|_{y=\mathcal{Y}(x)} + 2\, C^i{}_{j\ell}\frac{\partial y^\ell}{\partial x^k} + C^i{}_{k\ell}\frac{\partial y^\ell}{\partial x^j} - C^i{}_{jk}\frac{\partial y^\ell}{\partial x^\ell}\bigg|_{y=\mathcal{Y}(x)}, \tag{16}$$

where $C^i{}_{jk}$ is the Cartan torsion.

If a nowhere-vanishing tangent field $\mathcal{Y}(x)$ exists, the osculating Riemannian manifold $(M, g_{ij}(x))$ can be defined by $g_{ij}(x) = g_{ij}(x, y)\big|_{y=\mathcal{Y}(x)}$, in this osculating region the Cartan tensor vanishes, and the equation (16) reduces to

$$\gamma^i{}_{jk}(x) = \gamma^i{}_{jk}(x, y)\big|_{y=\mathcal{Y}(x)}, \tag{17}$$

so that the geodesic equation takes the Riemannian-like form

$$\frac{d^2x^i}{ds^2} + \gamma^i{}_{jk}(x)\, y^j y^k = 0. \tag{18}$$

In the context of the present study, the large-scale Universe is well described by a homogeneous and isotropic background. Under these conditions, velocity-dependent contributions from the torsion can only appear through isotropy-preserving background functions and their derivatives, which do not generate leading-order directional effects. As a result, photon trajectories can be modeled as null geodesics of the osculating Riemannian metric with any residual anisotropic corrections remaining well below current observational sensitivity, typically at the sub-percent level in the luminosity–distance relation.The resulting reduction ensures continuity with the standard Riemannian limit while retaining the leading anisotropic corrections relevant to cosmological evolution.

2.5 Barthel connection and the associated osculating Riemannian structure

Within the osculating Riemannian approach all Finslerian quantities are evaluated along the vector field $\mathcal{Y}(x)$ on the base manifold. In this context the Cartan torsion tensor C^i_{jk}, which captures the intrinsic non-Riemannian features of the Finsler space vanishes identically for a Riemannian metric or for those sections where the metric becomes direction-independent. As a result in the osculating region, the Barthel connection coefficients defined as in Eq. (6) reduces to

$$b^i_{kh} = \gamma^i_{kh}, \tag{19}$$

where, γ^i_{kh} are the standard Christoffel symbols are as defined in Eq. (12) and is evaluated using the osculating Riemannian metric. This bridges the Finslerian and Riemannian geometries and in the effective field equations and curvature calculations, the connection coefficients are given by the usual Riemannian expressions along the selected direction field. Consequently, the curvature tensor, Ricci tensor and scalar curvature appearing in the subsequent equations are to be interpreted as those of the osculating Riemannian manifold ensuring consistency with the Barthel framework.

Thus, for a Barthel connection (affine connection in osculating regions) in general the curvature tensor as defined in Eq. (10) reduces to

$$R^a_{bcd} = \frac{\partial \Gamma^a_{bd}}{\partial x^c} - \frac{\partial \Gamma^a_{bc}}{\partial x^d} + \Gamma^e_{bd}\Gamma^a_{ec} - \Gamma^e_{bc}\Gamma^a_{ed}, \tag{20}$$

where Γ^a_{bc} are the connection coefficients. The associated Ricci tensor and scalar curvature are defined as

$$R_{bd} = \sum_a \left(\frac{\partial \Gamma^a_{bd}}{\partial x^a} - \frac{\partial \Gamma^a_{ba}}{\partial x^d} + \sum_e \left(\Gamma^e_{bd}\Gamma^a_{ea} - \Gamma^e_{ba}\Gamma^a_{ed} \right) \right), \tag{21}$$

$$R = R^a_{bad}, \quad R^b_d = g^{bc} R_{cd}. \tag{22}$$

2.6 Kropina spaces

The Finsler metric is called an (α, β)-metric if the fundamental function $L(x, y) = \frac{F^2}{2}$ is 1-homogeneous in two arguments α, β defined by [46]

$$\alpha(x, y) = \sqrt{a_{ij}(x) y^i y^j}, \quad \beta = A_i(x) y^i. \tag{23}$$

where α represents a Riemannian metric and $\beta = A_i(x)y^i$ is a linear one-form on the tangent bundle TM on M, $A_i(x)$ is a directional vector field.

The Kropina metric is a special form of (α, β)-metric defined as [40–42]

$$L(x, y) = \frac{\alpha^2}{\beta} = \frac{a_{ij}(x) y^i y^j}{A_i(x) y^i}. \tag{24}$$

In view of Eqs. (24) and (1) the fundamental metric tensor for Finsler–Kropina space becomes

$$\hat{g}_{ij}(x, y) = \frac{L_\alpha}{\alpha} h_{ij} + \frac{L_{\alpha\alpha}}{\alpha^2} y_i y_j + \frac{L_{\alpha\beta}}{\alpha}(y_i A_j + y_j A_i) + L_{\beta\beta} A_i A_j, \tag{25}$$

where $h_{ij} = a_{ij} - \frac{y_i y_j}{\alpha^2}$ is the angular metric tensor of the associated Riemannian space and $L_\alpha = \frac{\partial L}{\partial \alpha}$ and $L_{\alpha\beta} = \frac{\partial^2 L}{\partial \alpha \partial \beta}$ and so on.

Recently, Bouali et al. [40,41] investigated the dark energy model based on the Finsler geometry-inspired osculating Barthel–Kropina background and showed that it gives a good description of the observational data, and it can be considered a viable alternative of the Λ-CDM model. The Barthel connection is employed within Finsler–Kropina geometry to incorporate vector field-induced Finslerian corrections. At every point x^i, the vector field $Y(x)$ characterizes the gravitational configuration, allowing the Barthel connection to serve a role analogous to that of the Levi–Civita connection within the osculating metric framework. This facilitates the formulation of anisotropic field equations and the investigation of cosmic dynamics. Within this framework the Christoffel symbols as expressed in Eq. (7) are obtained from the Y-osculating metric and the resulting affine structures facilitate a more transparent and computationally efficient treatment of curvature and other geometric quantities in Kropina spaces.

3 Gravitational field equations in Finsler–Barthel–Kropina space-time

This section develops the gravitational field equations for a cosmological model based on the Finsler–Barthel–Kropina geometric framework. By extending the standard FLRW metric we systematically incorporate anisotropic corrections and derive the corresponding dynamical equations governing the universe evolution.

To establish the Finsler–Barthel–Kropina cosmological model, we follow the procedure as carried out in [40–42] by specifying the underlying Riemannian metric in the Kropina structure, which is taken as

$$a_{ij}(x) = \text{diag}\left[1, -a^2, -a^2, -a^2\right], \tag{26}$$

where $a = a(t)$ is the cosmological scale factor describing homogeneous and isotropic evolution, and $i, j = 0, 1, 2, 3$.

The Finsler–Kropina metric depends on two main building blocks: the Riemannian part $\alpha(x, y) = \sqrt{a_{ij}(x)y^i y^j}$ and a preferred 1-form $\beta(x, y) = A_i(x)y^i$, which introduces a globally preferred direction in the geometry. For cosmological symmetry, we consider the parametrization vector field A_i as follows:

$$A_i(x) = (\eta(t), 0, 0, 0), \tag{27}$$

where $\eta(t)$ is a time-dependent function encoding the dynamical anisotropy.

To analyze physical predictions in a cosmological context we utilize the osculating Riemannian approach [43, 45] which enables the mapping of intrinsically direction-dependent Finslerian structures onto the spacetime manifold by evaluating all geometric quantities along a smooth non-zero vector field $Y^i(x) = A^i(x)$. Such a prescription is well established in Finsler gravity and allows us to treat anisotropic corrections while preserving computational traceability ([40,41] and references there in.) Applying the osculating Riemannian approach, we have the following:

$$\alpha(x, y)\big|_{y=A(x)} = \sqrt{a_{ij}(x)A^i(x)A^j(x)} = \eta(t) \tag{28}$$

$$\begin{aligned}\beta(x, y)\big|_{y=A(x)} &= A_i(x)A^i(x) = a_{ij}(x)A^i(x)A^j(x)\\ &= (\eta(t))^2\end{aligned} \tag{29}$$

Thus, using the osculating Riemannian approach, the general form of the Finsler–Barthel–Kropina metric tensor (25) can be rewritten as

$$\begin{aligned}\hat{g}_{ij}(x, y) = &\frac{2\alpha^2}{\beta^2}a_{ij}(x) + \frac{3\alpha^4}{\beta^4}A_i(x)A_j(x)\\ &-\frac{8\alpha^2}{\beta^3}A_iA_j(x) + \frac{4A_iA_j}{\beta^2},\end{aligned} \tag{30}$$

where y^i is replaced everywhere by $A^i(x)$ in the osculating prescription.

Substituting (28) and (29) in the Eq. (30), we obtain the non-vanishing components of $\hat{g}_{ij}$ are

$$\hat{g}_{00}(x, y) = \frac{1}{\eta(t)^2} \tag{31}$$

$$\hat{g}_{ij}(x, y) = -\frac{2a(t)^2}{\eta(t)^2}\delta_{ij}, \quad i, j = 1, 2, 3. \tag{32}$$

and $g_{0i} = 0, i = 1, 2, 3$.

Thus, the effective Finsler–Barthel–Kropina metric relevant for cosmology is

$$\hat{g}_{ij}(x, y) = \text{diag}\left(\frac{1}{\eta(t)^2}, -\frac{2a(t)^2}{\eta(t)^2}, -\frac{2a(t)^2}{\eta(t)^2}, -\frac{2a(t)^2}{\eta(t)^2}\right). \tag{33}$$

This result follows rigorously from the osculating Riemannian procedure applied to the Kropina metric obtained using non-vanishing vector field $A^i(x)$. The metric is non-degenerate as long as $\eta(t) \neq 0$. We note that our metric and modified Friedmann equations extended the works of [40,41] due to the choice of the privileged vector field $A_i = (\eta(t), 0, 0, 0)$ and by setting $\eta(t) \to a(t)\eta'(t)$ in above expressions, one can recover the form adopted by Bouali et al. [41].

In the Finsler–Barthel–Kropina metric (33), the scale factor $a(t)$ is a coordinate-dependent and $\eta(t)$ originates from the vector field component which is inherently independent of the coordinate system. This exhibits the fundamental role of $\eta(t)$ in introducing anisotropic corrections to the traditional FLRW cosmological model. Unlike $a(t)$, which can be transformed through coordinate transformations, $\eta(t)$ encapsulates the physical influence of the vector field modifying the metric and dynamically influencing the evolution equations. Consequently, $\eta(t)$ cannot be absorbed into $a(t)$ by coordinate transformations as it represents a distinct geometric feature that drives anisotropic effects and alters the behavior of key cosmological parameters, such as the Hubble parameter, deceleration parameter, and energy conditions. This inherent anisotropy offers novel perspectives on departures from the standard FRLW cosmological model.

For Finsler–Barthel–Kropina space-time the action is given by

$$S = \int dx^4\sqrt{-\hat{g}}\left(\frac{1}{2\kappa}\hat{R} + L_m\right), \tag{34}$$

where $\sqrt{-\hat{g}}$ is the determinant of the osculating Barthel–Kropina–Finsler metric (33), $\hat{R}$ is the corresponding Ricci scalar and L_m is matter Lagrangian.

By varying the action (34) with respect to the metric (33) we obtain the gravitational field equations as [40–42]

$$\hat{R}_{ij} - \frac{1}{2}\hat{g}_{ij}\hat{R} = k\hat{T}_{ij}, \tag{35}$$

where $\hat{R}_{ij}$ and denote the Ricci tensor and Ricci scalar as defined in (21) and (22) respectively and $k = \frac{8\pi G}{c^4}$ which is taken to be unity throughout the study. $\hat{T}_{ij}$ denotes the energy-momentum tensor, is given by

$$\hat{T}_{ij} = \text{diag}\left(\hat{g}_{00}\rho, -\hat{g}_{11}p, -\hat{g}_{22}p, -\hat{g}_{33}p\right), \tag{36}$$

where ρ and p respectively are the energy density and pressure of the matter distribution of the universe.

The components of the Ricci tensor are obtained using the Eq. (21) as

$$R_{00} = \frac{-3\ddot{a}\eta^2 + 3\ddot{\eta}\eta a + 3\eta\dot{a}\dot{\eta} - 3a\dot{\eta}^2}{a\eta^2}, \tag{37}$$

$$R_{11} = R_{22} = R_{33} = \frac{2\ddot{a}\eta^2 a - 2\ddot{\eta}\eta a^2 + 4\eta^2\dot{a}^2 - 10\eta a\dot{a}\dot{\eta} + 6a^2\dot{\eta}^2}{\eta^2}. \tag{38}$$

Then by using (22) the Ricci scalar is calculated as

$$R = -\frac{6\left(\ddot{a}\eta^2 a - \ddot{\eta}\eta a^2 + \eta^2\dot{a}^2 - 3\eta a\dot{a}\dot{\eta} + 2a^2\dot{\eta}^2\right)}{a^2}. \tag{39}$$

In view of Eqs. (33)–(39) the generalized Friedmann equations for Finsler–Barthel–Kropina background are obtained as

$$3\dot{\eta}^2 + 3\eta^2 H^2 - 6\eta\dot{\eta}H = \rho \tag{40}$$

$$-3\dot{\eta}^2 - 3\eta^2 H^2 + 4\eta\dot{\eta}H - 2\eta^2\dot{H} + 2\eta\ddot{\eta} = p \tag{41}$$

here the dot represents differentiation with respect to time t.

The Eqs. (40)–(41) describe respectively the energy density ρ and pressure p to the Hubble parameter H and anisotropy parameter $\eta(t)$ providing a comprehensive view of the dynamics of universe and its structure.

Further the conservation law of the energy-momentum tensor $\hat{T}^{j}_{i;j} = 0$ leads to the following equation

$$\dot{\rho} + 3\left(\frac{\dot{a}}{a} - \frac{\dot{\eta}}{\eta}\right)(\rho + p) = 0, \tag{42}$$

where semicolon (;) denotes covariant differentiation, $H{=}\frac{\dot{a}}{a}$ describes the Hubble parameter, describing the expansion rate of the universe, and $\frac{\dot{\eta}}{\eta}$ accounts for the additional geometric modifications introduced by the Finslerian correction. This conservation equation, derived from the Barthel–Kropina–Finsler metric, offers valuable insights into cosmological evolution.

The inclusion of $\eta(t)$ is particularly significant as it captures the anisotropic nature of the universe in a Finslerian space-time. This correction influences the evolution of energy density ρ and pressure p, reflecting how these quantities are interrelated not only through the expansion dynamics but also through the geometric properties of the underlying space-time. Consequently, the rate of change of energy density becomes dependent on both the H and the Finslerian term η, which allows for a richer and more detailed understanding of the universe evolution and its response to varying conditions. In particular as $\eta \to 1$, the Eqs. (40)–(41) reduce to the standard Friedmann equations of general relativity.

4 Methodology and observational data analysis

In the present investigation we employ the Chi-square test and the Markov Chain Monte Carlo (MCMC) analysis to estimate the posterior distributions of the model parameters in accordance with observational data. The Chi-square test is used to assess the goodness of fit between theoretical cosmological models and observational datasets and the MCMC method systematically explores the parameter space by generating a sequence of samples, where model predictions are iteratively compared with observational data. Rather than providing a single best-fit value, MCMC yields a distribution of plausible parameter values, allowing for a rigorous quantification of uncertainties and a robust comparison of competing models. To constrain the posterior distributions, we incorporate the set of observational data including cosmic chronometers (CC), baryon acoustic oscillations (BAO), Type Ia Supernovae (SNe Ia), and the latest Pantheon+ compilation derived from supernova observations.

4.1 Cosmic chronometers (CC) dataset

The cosmic chronometer (CC) method is a valuable approach for determining the Hubble rate by examining the oldest and most passively evolving galaxies. These galaxies are carefully selected based on a narrow redshift interval, which allows for the application of the differential aging method. The Hubble parameter $H(z)$ is defined by the relationship [50–55]

$$H(z) = -\frac{1}{1+z}\frac{dz}{dt}. \tag{43}$$

The Eq. (43) enables the deduction of the universe expansion rate at various epochs, providing a measure of the Hubble parameter without reliance on specific cosmological assumptions. In this study, we use 31-data points collected through the CC technique, which directly extracts information about the Hubble parameter at various redshifts up to $z \leq 2$ ([54,55] and references therein). This method relies on measurements of age differences between two passively evolving galaxies that originated simultaneously but are separated by a small redshift interval and allows us to compute $\frac{dz}{dt}$ accurately.

For the analysis we employ the Chi-square (χ^2) function to assess the best fit of our model against the observed data and is given by

$$\chi^2_{Hz}(H_0) = \sum_{k=1}^{31} \frac{[H_{th}(z_k, H_0) - H_{obs}(z_k)]^2}{\sigma_H^2(z_k)}, \tag{44}$$

where H_{th} and H_{obs} denote the theoretical estimated value and observed values of the Hubble parameter respectively and σ_H represents the associated error in the measurement. By minimizing the χ^2-values, we can constrain the parameters of the model effectively enhancing our understanding of the universe expansion history.

4.2 Baryon acoustic oscillations (BAO) dataset

Baryon acoustic oscillations (BAO) act as cosmic standard rulers, revealing the imprint of sound waves from the early universe photon-baryon plasma. These sound waves were frozen in the large-scale galaxy distribution, offering a precise measure of the cosmic expansion history [52–56]. BAO helps determine the Hubble parameter through the relation $H(z_i)r_d$, where $r_d = 147.74$ Mpc represents the sound horizon at the drag epoch in the ΛCDM model. In this study, we have chosen 26 uncorrelated-BAO data points within the redshift range $0.24 < z < 2.36$ [53–55].

The χ^2 statistics for the BAO dataset are given as,

$$\chi^2_{\rm BAO} = \sum_{i=1}^{26} \frac{(H(z_i) - H_{\rm BAO}(z_i))^2}{\sigma^2_{\rm BAO}(z_i)}, \tag{45}$$

where $H(z_i)$ and $H_{\rm BAO}(z_i)$ respectively describe the theoretically estimated and observed value expansion rate (H) at redshift z_i, and $\sigma_{\rm BAO}(z_i)$ represents the associated uncertainty.

For the combined CC and BAO datasets, the total χ^2 function is given by

$$\chi^2_{\rm CC+BAO} = \chi^2_{\rm CC} + \chi^2_{\rm BAO}. \tag{46}$$

4.3 Pantheon+ dataset

The *Pantheon+* dataset is an enhanced and comprehensive collection of Type Ia Supernovae (SNe Ia) data, building on the earlier Pantheon dataset. It includes light curves from 1701 observations of 1550 unique SNeIa, spanning a wide redshift range from $0.001 \leq z \leq 2.2613$ ([54,55] and references therein). In this study, we used these data points to constrain our model parameters. This improvement is particularly important, as it incorporates 77 SNe Ia associated with galaxies hosting Cepheid variables, crucial for refining measurements of the Hubble constant H_0, and resolving parameter degeneracies in the cosmological model.

For each supernova, the distance modulus μ_i is calculated by comparing the apparent magnitude $m_{B,i}$ to the absolute magnitude M,

$$\mu_i = m_{B,i} - M. \tag{47}$$

where M the absolute magnitude is often treated as a nuisance parameter, influencing the overall brightness scale.

The luminosity distance $d_L(z)$, which is derived from the redshift z and the Hubble parameter $H(z)$, follows

$$d_L(z, \theta) = c(1+z) \int_0^z \frac{d\xi}{H(\xi)} \tag{48}$$

where c denotes the speed of light. The theoretical distance modulus $\mu_{\rm th}$ is given as

$$\mu_{\rm th}(z, \theta) = 5 \log_{10}\left(\frac{d_L(z, \theta)}{1\ {\rm Mpc}}\right) + 25 \tag{49}$$

To estimate the cosmological parameters, the *Pantheon+* dataset uses the χ^2 minimization method. The Chi-square function $\chi^2_{\rm SNe\ Ia}$ compares the observed distance moduli μ_i with the theoretical values $\mu_{\rm th}(z_i)$ for each supernova,

$$\chi^2_{\rm SNeIa} = \Delta\mu^T \left(C^{-1}_{\rm stat+sys}\right) \Delta\mu, \tag{50}$$

where $\Delta\mu_i = \mu_i - \mu_{\rm th}(z_i)$, and $C_{\rm stat+sys}$ is the covariance matrix, which accounts for both statistical and systematic uncertainties such as intrinsic scatter, peculiar velocities, and redshift uncertainties. A known limitation when using SNe Ia data alone is the degeneracy between the Hubble constant H_0 and the absolute magnitude M, which restricts the precision of H_0 estimates. In this work, M is treated as an additional free parameter and is fitted simultaneously with the other cosmological parameters in the MCMC analysis, allowing the dataset to determine its best-fit value without imposing an external prior.

For a more robust analysis, the *Pantheon+* data is often combined with other cosmological probes such as *CC* and *BAO*. In such cases, the total χ^2-function is the sum of contributions from each dataset

$$\chi^2_{\rm tot} = \chi^2_{\rm CC} + \chi^2_{\rm BAO} + \chi^2_{\rm SNeIa} \tag{51}$$

To explore the parameter space and find the best-fit cosmological parameters, a *Markov-Chain-Monte-Carlo (MCMC)* method is employed. This method iterates through possible values of parameters to minimize χ^2, or equivalently, to maximize the likelihood function

$$L \propto \exp\left(-\frac{\chi^2}{2}\right) \tag{52}$$

5 Parametrization of anisotropic parameter (η) and the models

From the Eqs. (40)–(41) one encounters a scenario where the system is undetermined because of two independent differential equations containing four unknowns – ρ, p, H, η. This necessitates two specific additional parametrizations or constraints to render the system solvable.

The parametrization of the anisotropy function η is fundamental for examining its role in cosmic evolution and structure formation within Finslerian cosmology [24,26–28]. In these models η quantifies deviations from the standard isotropic framework of general relativity, thereby modifying the dynamics of cosmic expansion and the growth of structure. To enable direct comparison with observational data, it is natural to express it as a function of redshift z, which leads to a general Taylor expansion [28,50,53,56]

$$\eta(z) = \eta(0) + z\eta'(0) + \frac{1}{2}z^2\eta''(0) + \cdots \tag{53}$$

where $\eta(0)$ encodes the present-day value of anisotropy, and $\eta'(0)$ describes its variation with redshift near $z = 0$. Physically higher-order terms are expected to be small at late times, especially if the underlying vector field responsible for anisotropy is weak or slowly varying in the current universe [19,25,34,35]. This motivates the adoption of a linear approximation for $\eta(z)$ as the simplest nontrivial extension to the standard model and is given by [56]

$$\eta(z) = 1 + nz, \tag{54}$$

where the parameter n controls the rate of change of anisotropy with redshift and vanishes in the isotropic limit.

As discussed in [19,22,25,25,34,35] linear or first-order Taylor expansions are commonly employed to approximate time or redshift-dependent background fields when higher-order corrections are negligible at late times. Specifically, for Finslerian or spurionic vector fields the linearized ansatz (54) provides a valid late-time description under the assumption of weak Lorentz violation, where the higher derivatives of the field are subdominant [25,28]. This approach has been used to derive modified Friedmann equations for locally anisotropic universes with the anisotropy naturally fading away as the universe expands. As the universe evolves toward homogeneity and isotropy at late times the linearized parametrization remains both accurate and physically motivated capturing the dominant corrections without introducing unnecessary complexity or overfitting to limited data.

It is important to emphasize that our framework remains compatible with more general forms of $\eta(z)$, including polynomial and nonparametric representations which can be systematically explored as future observational constraints improve. For the purposes of this study, however the linear form ensures both analytic tractability and direct interpretability in confronting Finslerian anisotropy with current cosmological observations. This parametrization provides a clear avenue for investigating the possible influence of weak late-time anisotropy on key observables such as the Hubble parameter, energy density and cosmic acceleration [50–54].

Further the general solution of the conservation equation (42) is given by

$$\rho(t) = \rho_0 \exp\left\{-3\int_{t_0}^{t}[1+\omega(\tau)]\left(\frac{\dot{a}}{a} - \frac{\dot{\eta}}{\eta}\right)d\tau\right\} \tag{55}$$

where ρ_0 is an integration constant typically identified as the present-day energy density.

For each cosmological context, the equation of state (EoS) parameter $\omega = \frac{p}{\rho}$ takes a characteristic value: $\omega = 0$ for pressure-less matter (dust), $\omega = \frac{1}{3}$ for radiation, and $\omega = \omega_{de}$ for dark energy, where ω_{de} may be constant or a function of redshift.

The explicit forms of ω_{de} considered in this work are (i) constant value and (ii) the Chevallier–Polarski–Linder (CPL) parametrization, which allows us to compute the dark energy density evolution accordingly leading to the expressions for the Hubble parameter presented in the following models [13–15]:

- *Model 1: Constant EoS parameter* (ω_{de})
  For a constant EoS parameter ω_{de}, the conservation law leads to a modified scaling for energy density. The Hubble parameter is thus obtain as (from Eqs. (55) and (40)).

$$H(z) = H_0\sqrt{\frac{\Omega_m(1+z)^3(1+nz)^3 + \Omega_r(1+z)^4(1+nz)^4 + \Omega_{de}(1+z)^{3(1+\omega_{de})}(1+nz)^{3(1+\omega_{de})}}{(2nz+n+1)^2}} \tag{56}$$

  where H_0 is the present-day Hubble parameter and $\Omega_m = \rho_{m,0}/(3H_0^2)$ and $\Omega_r = \rho_{r,0}/(3H_0^2)$ are the present-day values of the matter and radiation density parameters respectively and n is the Finslerian anisotropy parameter The present day dark energy density parameter Ω_{de} is given by

$$\Omega_{de} = (n+1)^2 - \Omega_m - \Omega_r. \tag{57}$$

- *Model 2: CPL parametrization*
  The Chevallier–Polarski–Linder (CPL) parametrization is a widely recognized model in cosmology for describing the redshift evolution of the dark energy EoS [57,58]. In this framework, the EoS is expressed as

$$\omega_{\rm de}(z) = \omega_0 + \omega_1 \frac{z}{1+z} \tag{58}$$

where ω_0 denotes the present-day value of the ω and ω_1 represents its rate of change with redshift. The CPL approach is advantageous because it provides a smooth transition between early and late cosmological epochs remains well-behaved at high redshifts and effectively accommodates a range of observational data. By utilizing only two parameters, this model offers a straightforward yet powerful means to investigate possible departures from the cosmological constant scenario ($\omega = -1$) and to explore the dynamics of dark energy [57,58].

Table 1 Estimated cosmological parameters for the constant-ω_{de} (Model-1) Kropina framework using combined observational data

Parameter	CC+BAO	CC+BAO+SNIe
H_0 [km/s/Mpc]	69.97 ± 0.46	69.47 ± 0.44
Ω_m	0.296 ± 0.015	0.302 ± 0.018
Ω_r	$(8.54 \pm 0.11) \times 10^{-5}$	$(7.71 \pm 0.04) \times 10^{-5}$
n	0.025 ± 0.013	0.019 ± 0.015
ω_{de}	-1.00 ± 0.02	-0.98 ± 0.02
M	–	-19.385 ± 0.011

$$H(z) = H_0 \sqrt{\frac{\Omega_m (1+z)^3 (1+nz)^3 + \Omega_r (1+z)^4 (1+nz)^4 + \Omega_{de} \left[(1+z)(1+nz)\right]^{3(1+\omega_0+\omega_1)} \exp\left(-\frac{3\omega_1 z}{1+z}\right)}{(2nz+n+1)^2}}. \tag{59}$$

The Hubble parameter is then express as where Ω_{de} is defined by Eq. (57).

These parametrizations allow for direct confrontation of Finslerian models with cosmological data by connecting geometric corrections to observable quantities. The present work, therefore, constrains these parameters through cosmological observations, analyzing their impact on the expansion history and the anisotropic modifications introduced by the Finslerian framework.

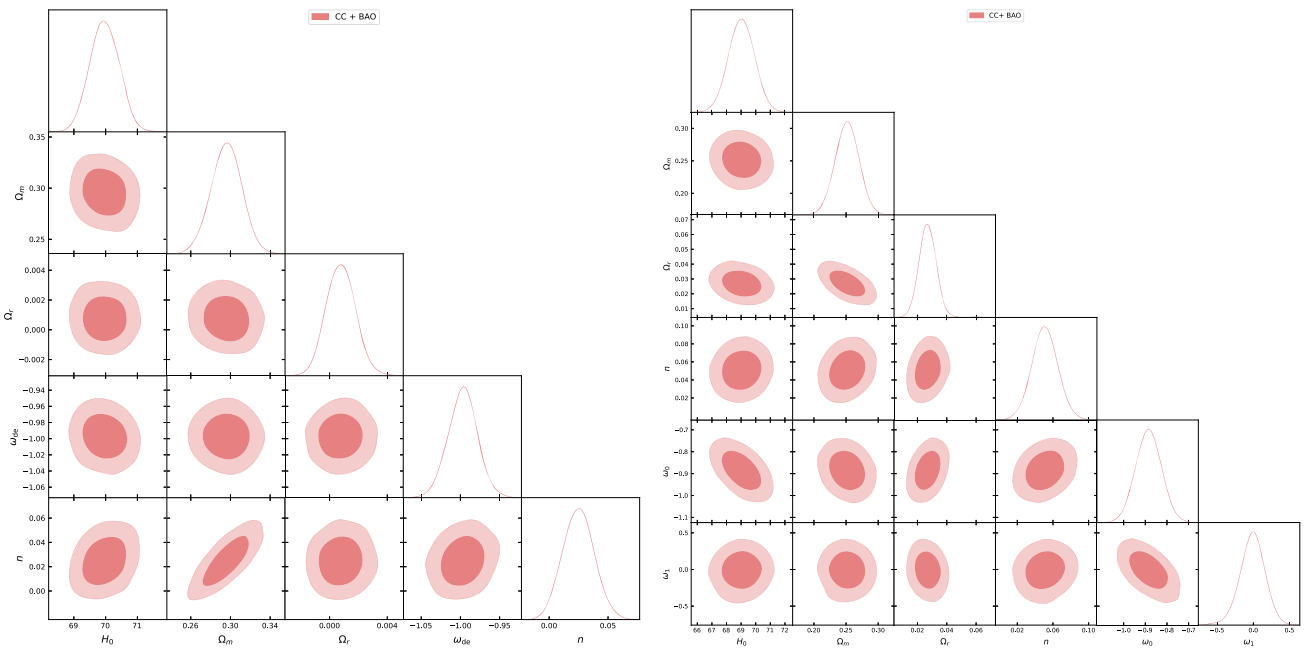

(a) Model-1 **(b)** Model-2

Fig. 1 Triangle plots illustrating the joint posterior distributions and parameter correlations for Model-1 and Model-2 obtained from the combined cosmic chronometer (CC) and Baryon acoustic oscillation (BAO)

6 Parameter estimation for Model-1 and Model-2: analysis through CC, BAO and SNe Ia observational data

In this section, we present the constraints on the key cosmological parameters of both Model-1 and Model-2 using recent cosmic chronometers (CC), baryon acoustic oscillations (BAO), and Supernovae Ia (SNe Ia) data. To ensure the reliability of our parameter estimation, we analyzed the convergence of our MCMC chains using the *Gelman–Rubin* statistics ($\hat{R}$) and the effective sample size (N_{eff}). For all parameters in each cosmological model,we find $\hat{R} < 1.01$ and $N_{\text{eff}} > 1000$, indicating convergence and adequate sampling of the posterior distributions.

6.1 Model-1: ω_{de} = constant

For the scenario with a constant equation of state, analysis using the CC+BAO dataset yields $H_0 = 69.97 \pm 0.46$ km/s/Mpc for the Hubble constant, with the matter and radiation density parameters determined to be $\Omega_m = 0.296 \pm 0.015$ and $\Omega_r = (8.54 \pm 0.11) \times 10^{-5}$, respectively. The Finslerian anisotropy parameter is constrained as $n = 0.025 \pm 0.013$, while the dark energy equation of state parameter is found to be $\omega_{de} = -1.00 \pm 0.02$, indicating a value close to the cosmological constant. When the SNe Ia sample is incorporated in the joint CC+BAO+SNIe analysis, the Hubble constant becomes $H_0 = 69.47 \pm 0.44$ km/s/Mpc, and the matter density changes to $\Omega_m = 0.302 \pm 0.018$, with the radiation density reduced to $(7.71 \pm 0.04) \times 10^{-5}$. The anisotropy parameter slightly decreases to $n = 0.019 \pm 0.015$, and the equation of state parameter remains close to a cosmological constant at $\omega_{de} = -0.98 \pm 0.02$. These results reflect high-precision parameter estimates and indicate only mild evidence for late-time anisotropy within the Finslerian cosmological framework. Table 1 summarizes the best-fit parameter values for Model 1. The difference in H_0 estimates between the CC+BAO and CC+BAO+SNIe analyses is modest but reflects the general context of the Hubble tension, with our values lying between the lower Planck 2018 CMB-inferred estimate ($H_0 \approx 67.4$ km/s/Mpc) and the higher local SH0ES measurement ($H_0 \approx 73.0$ km/s/Mpc). For Model-1, the calibrated absolute magnitude is $M = -19.385 \pm 0.011$, which is slightly brighter than the SH0ES determination of $M = -19.253 \pm 0.027$ [59]. The best-fit for model parameters in Model 1 is presented in Triangular plots Fig. 1a and Fig. 2a.

6.2 Model-2: $\omega_{de}(z) = \omega_0 + \omega_1 \frac{z}{1+z}$

For the CPL parameterization, the CC+BAO dataset analysis constrains the Hubble constant to $H_0 = 69.03 \pm 0.89$ km/s/Mpc, with the matter density parameter $\Omega_m = 0.252 \pm 0.019$ and the radiation density $\Omega_r = (8.61 \pm 0.22) \times 10^{-5}$. The anisotropy parameter is found to be $n = 0.051 \pm 0.015$. The CPL dark energy equation of state parameters are $w_0 =$

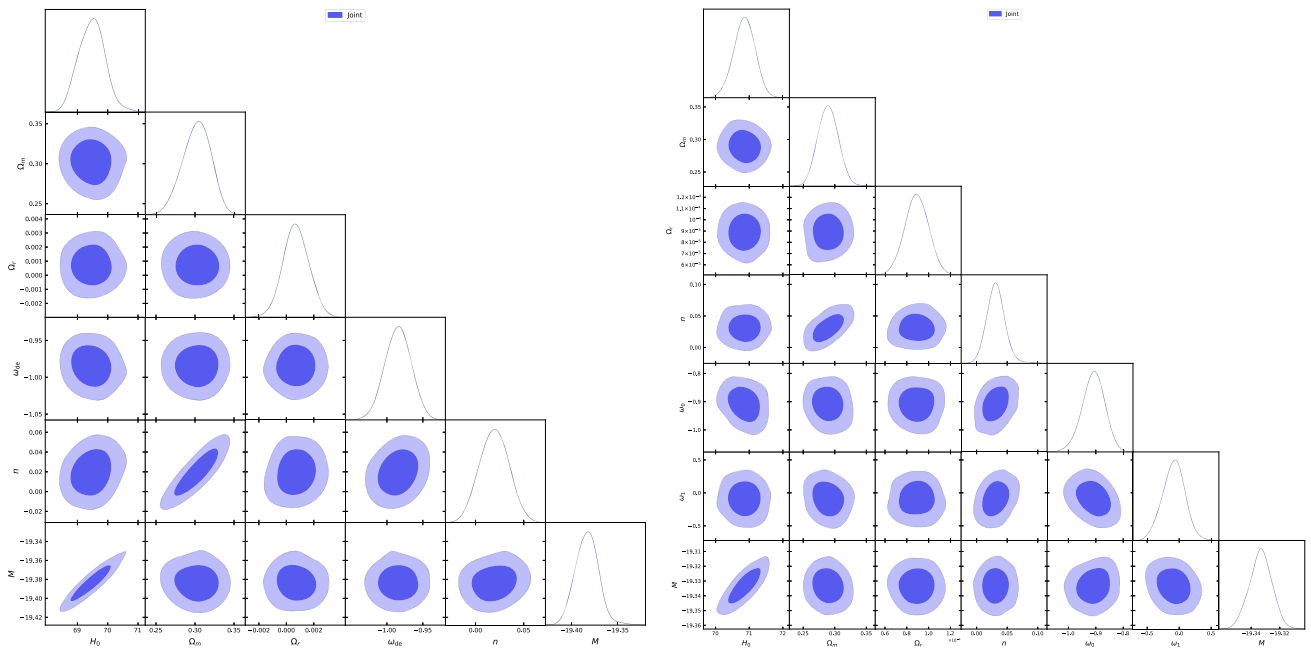

(a) Model-1 **(b)** Model-2

Fig. 2 Triangle plots illustrating the joint posterior distributions and parameter correlations for Model-1 and Model-2 obtained from the combined cosmic chronometer (CC), Baryon acoustic oscillation (BAO) and Pantheon+ supernova data

-0.885 ± 0.060 and $w_1 = -0.013\pm0.175$, indicating a value close to a cosmological constant with only mild evolution. The parameter constraints for Model 2, along with their best-fit as in global values, are illustrated in the triangular plots of Fig. 1b and Fig. 2b. When the SNe Ia data are included in the joint CC+BAO+SNIe analysis, the best-fit Hubble constant becomes $H_0 = 70.86 \pm 0.32$ km/s/Mpc, the matter density parameter increases to $\Omega_m = 0.289 \pm 0.016$, and the radiation density reduces to $\Omega_r = (7.65 \pm 0.05) \times 10^{-5}$. The anisotropy parameter is $n = 0.032 \pm 0.015$, while the CPL parameters are constrained to $\omega_0 = -0.909 \pm 0.041$ and $\omega_1 = -0.085 \pm 0.175$. Similar to Model-1, the difference in H_0 values between datasets reflects the Hubble tension: the CC+BAO result is closer to the CMB-inferred Planck value, while the CC+BAO+SNIe result moves toward the SH0ES measurement, indicating the model's flexibility in bridging the gap between these estimates. For Model-2, the corresponding value is $M = -19.333 \pm 0.079$, also lying within 2σ consistency with the SH0ES calibration [59]. The results of the best-fit analysis for Model 2 parameters are given in Table 2.

Table 2 Estimated cosmological parameters for the CPL-ω_{de} (Model-2) Kropina framework using combined observational data

Parameter	CC+BAO	CC+BAO+SNIe
H_0 [km/s/Mpc]	69.03 ± 0.89	70.86 ± 0.32
Ω_m	0.252 ± 0.019	0.289 ± 0.016
Ω_r	$(8.61 \pm 0.22) \times 10^{-5}$	$(7.65 \pm 0.05) \times 10^{-5}$
n	0.051 ± 0.015	0.032 ± 0.015
w_0	-0.885 ± 0.060	-0.909 ± 0.041
w_1	-0.013 ± 0.175	-0.085 ± 0.175
M	–	-19.333 ± 0.079

6.3 Observational and theoretical comparisons of the Hubble function and distance modulus

6.3.1 Hubble parameter

Figure 3 presents a comparison of the Hubble parameter $H(z)$ as a function of redshift for both Model-1 and Model-2, along with the CC and BAO data. For Model-1 the theoretical $H(z)$ curve closely tracks the observational data across the redshift range with especially good agreement at low and intermediate redshifts. This confirms that a constant EoS parameter combined with the Finslerian anisotropy parameter n can also reproduce the observed expansion history within uncertainties. For Model-2 the $H(z)$ prediction also provides an excellent fit to the data with the evolving CPL parameterization allowing for subtle variations at higher redshift. The Model-2 curve shows a marginally better agreement with the BAO data points at $z > 1$, capturing possible late-time departures from ΛCDM. Both models provide a satisfactory description of the observed Hubble expansion history, but Model-2 demonstrates slightly improved performance at higher redshift reflecting the physical relevance of a time-dependent dark energy component.

6.3.2 Distance modulus

The distance modulus $\mu(z)$ provides a direct comparison between theoretical predictions and observed supernova data over a wide range of redshifts. Figure 4 illustrate that both Model-1 and Model-2 accurately capture the observed trend of increasing apparent magnitude with redshift consistent with the expected dimming of distant sources in an expanding universe.

For Model-1 the theoretical distance modulus is given by

$$\mu^{(1)}_{\rm th}(z) = 5\log_{10}\left[c\frac{(1+z)}{H_0}\int_0^z \frac{2nx+n+1}{\sqrt{\Omega_m(1+x)^3(nx+1)^3+\Omega_r(1+x)^4(nx+1)^4+\Omega_{de}(1+x)^{3(1+\omega_{de})}(nx+1)^{3(1+\omega_{de})}}}dx\right]+25. \tag{60}$$

For Model-2 the distance modulus is given by

$$\mu^{(2)}_{\rm th}(z) = 5\log_{10}\left[c\frac{(1+z)}{H_0}\int_0^z \frac{2nx+n+1}{\sqrt{\Omega_m(1+x)^3(nx+1)^3+\Omega_r(1+x)^4(nx+1)^4+\Omega_{de}\,[(1+x)(nx+1)]^{3(1+\omega_0+\omega_1)}\,e^{-3\omega_1 x/(1+x)}}}dx\right]+25. \tag{61}$$

In Model-1 the theoretical prediction for the distance modulus $\mu(z)$ demonstrates close agreement with the Pantheon+ supernova dataset across low and intermediate redshifts. Model-2 incorporating a redshift-dependent equation of state displays comparable performance at these redshifts while providing a marginally improved correspondence with observations at higher redshifts ($z > 1$).

7 Physical viability of the models and cosmographic parameters

In this section we evaluates the physical viability of the proposed Finsler-Barthel-Kropina cosmological models by ana-

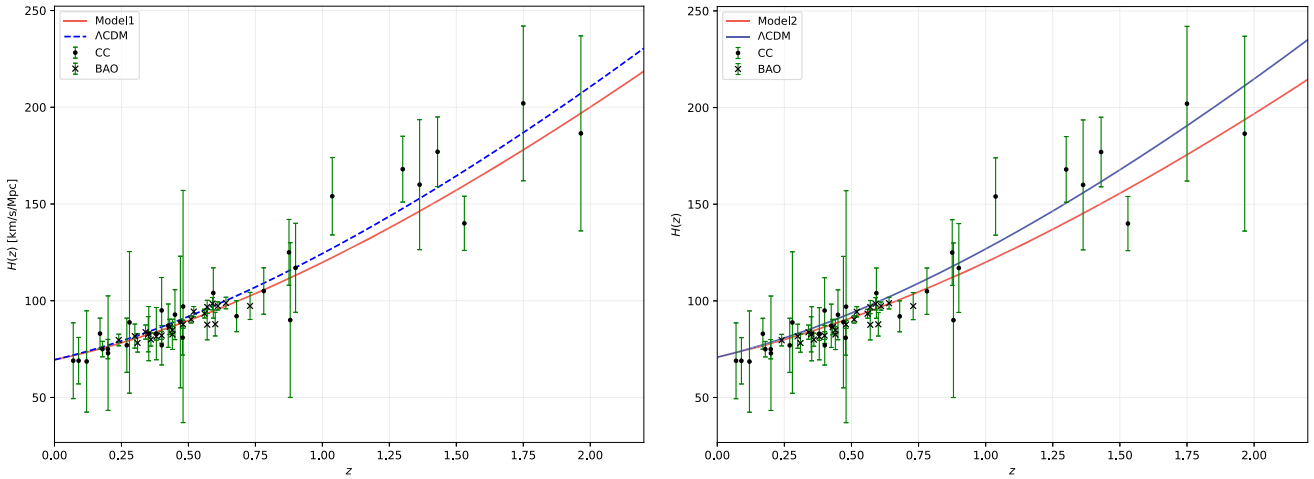

(a) Model-1 **(b)** Model-2

Fig. 3 Reconstructed Hubble parameter $H(z)$ for Model-1 (left) and Model-2 (right), shown alongside observational data from cosmic chronometers (CC) and baryon acoustic oscillations (BAO)

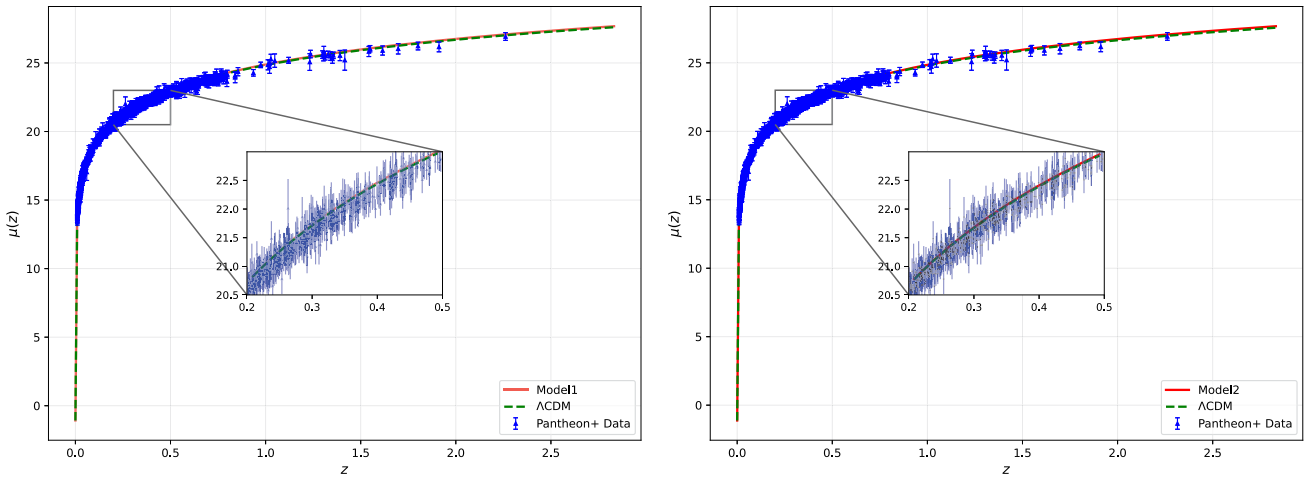

(a) Model-1 **(b)** Model-2

Fig. 4 Comparison of the theoretical distance modulus $\mu(z)$ for Model-1 (left) and Model-2 (right) with observational data from Type Ia Supernovae

lyzing their compliance with standard energy conditions and comparing key cosmographic parameters.

7.1 Energy conditions

The energy conditions (EC) play a crucial role in assessing the physical plausibility of cosmological models. They are defined as follows:

- Null energy condition (NEC): $\rho + p \geq 0$.
- Weak energy condition (WEC): $\rho \geq 0, \quad \rho + p \geq 0$.
- Strong energy condition (SEC): $\rho + p \geq 0$, $\rho + 3p \geq 0$.
- Dominant energy condition (DEC): $\rho \geq 0, \quad \rho \geq |p|$.

The evolution of energy density and pressure for both Model-1 and Model-2 are graphically analyzed in Fig. 5 and is broadly consistent with standard cosmological expectations. For both models, the energy density ρ remains positive across the entire redshift range, and the combinations $\rho + p$ and $\rho + p$ also stay positive, confirming that the dominant and null energy conditions are satisfied throughout. However, the quantity $\rho + 3p$ becomes negative at low redshifts in both models highlighting a violation of the strong energy condition. This behavior is typical for cosmological scenarios featuring accelerated expansion, where dark energy or a cosmological constant dominates at late times.

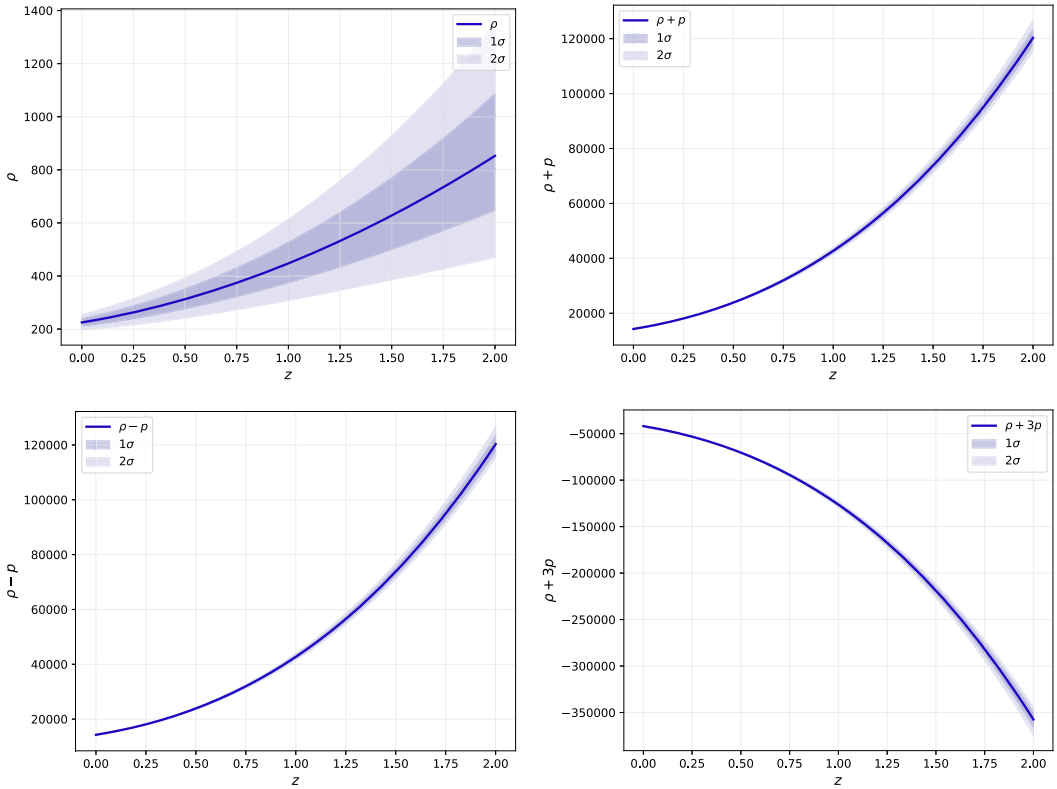

(a) Model-1

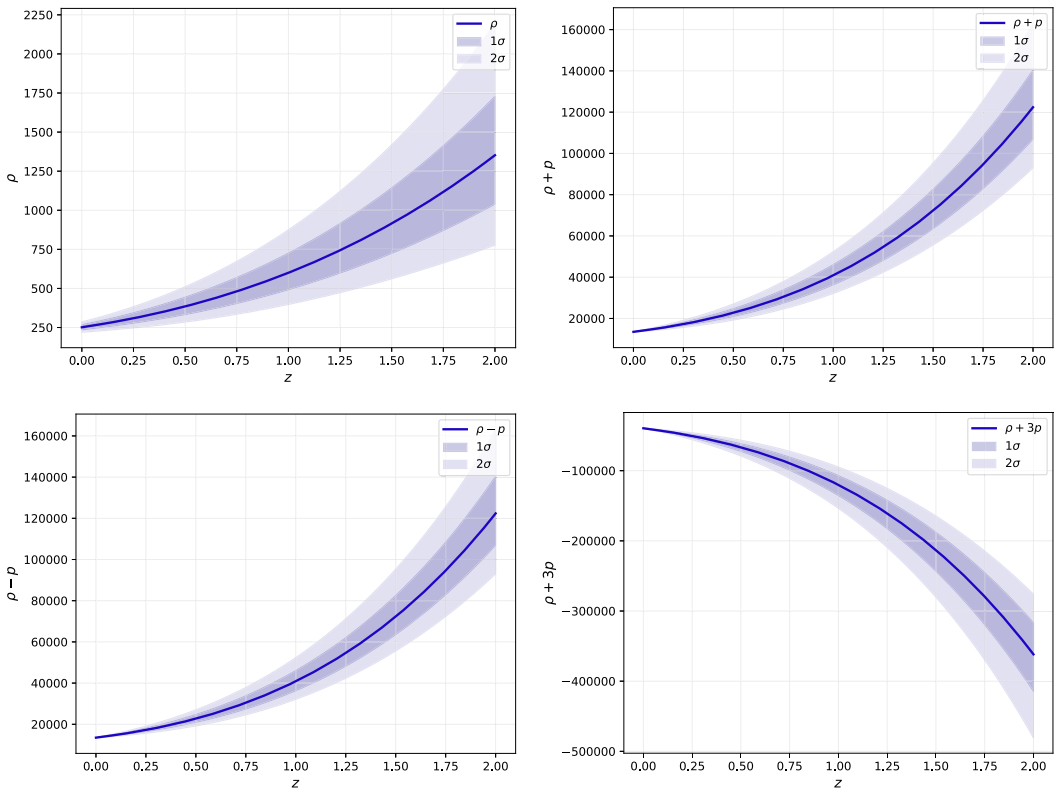

(b) Model-2

Fig. 5 Energy condition analysis for Model-1 and Model-2 using combined best-fit values from observational data for the parameters

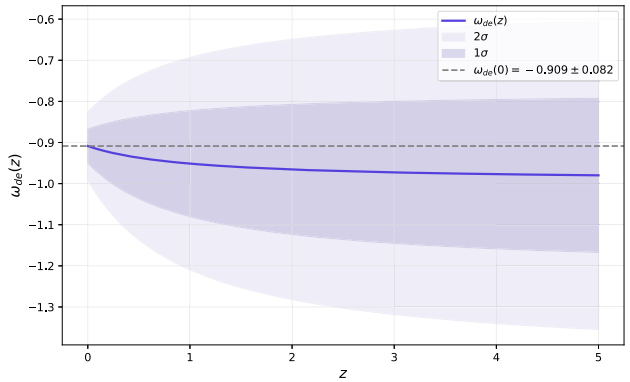

Fig. 6 Redshift evolution of the dark energy equation-of-state parameter $\omega_{de}(z)$ for Model-2 following the CPL parameterization

7.2 Equation of state

Figure 6 presents the evolution of the dark energy equation of state parameter $\omega_{de}(z)$ for Model-2 utilizing the CPL parametrization. The curve shows that $\omega_{de}(z)$ is consistently negative across all redshifts considered, with a present-day value of $\omega_{de}(0) = -0.909 \pm 0.082$. This is close to the cosmological constant value ($\omega_{de} = -1$), suggesting a dark energy component. This result indicates that, while Model-2 allows for a mild temporal variation in the dark energy equation of state, the behavior is largely consistent with observational data. In contrast, Model-1 assumes a strictly constant $\omega_{de} = -0.98 \pm 0.02$, resulting in a flat, non-evolving EoS parameter across cosmic history.

7.3 Deceleration parameter

The deceleration parameter characterizes the expansion dynamics of the universe with negative values indicating acceleration. For Model-1 the present value is found to be $q(0) = -0.58 \pm 0.03$ with the transition from deceleration to acceleration occurring at $z_{\rm tr} = 0.72 \pm 0.024$ as refereed in Fig. 7a. Similarly, Model-2 Fig. 7b yields a present value $q(0) = -0.54 \pm 0.09$ and a transition redshift of $z_{\rm tr} = 0.82 \pm 0.011$. Both models successfully capture the universe transition from decelerated to accelerated expansion, with the transition points lying within the expected observational range. The close agreement in $q(0)$ and $z_{\rm tr}$ between the two models demonstrates the robustness of these Finslerian cosmological scenarios in describing late-time acceleration.

7.4 Jerk parameter

The jerk parameter provides insight into the rate of change of the universe acceleration. For Model-1, the present value is $j(0) = 0.996$ as shown in Fig. 8a indicating a pronounced deviation from the standard ΛCDM value of unity and suggesting enhanced dynamical features in cosmic acceleration. For Model-2, the jerk parameter at the present epoch is $j(0) = 0.69$ as indicated in Fig. 8(b) reflecting a dynamic departure from ΛCDM in which $j(0) = 1$.

7.5 Snap parameter

The snap parameter gives the higher-order time evolution of the universe expansion. For Model-1, the current value is found to be $s(0) = -0.297$ indicating a mild negative contribution to the cosmic expansion at the present epoch as depicted in Fig. 9a. In Model-2, the snap parameter at present is even more negative $s(0) = -0.86$ suggesting a more pronounced deviation from the standard cosmological constant scenario where $s(0) = 0$ and is illustrated as in Fig. 9b.

7.6 Om(z) diagnostic analysis of the models

The $Om(z)$ diagnostic provides a powerful tool for distinguishing between cosmological models by assessing the evolution of the Hubble parameter as a function of redshift. For Model-1, as depicted in Fig. 10a, $Om(z)$ remains nearly constant over the entire redshift range with values clustered tightly around $\Omega_{m,0} \simeq 0.27$. This flat behavior is characteristic of the standard ΛCDM model and indicates that Model-1 closely mimics a cosmological constant scenario with no significant evidence for dynamic dark energy or interaction effects in the current data. In contrast Model-2 as depicted in Fig. 10b displays a decreased nature of $Om(z)$ with increasing redshift. This negative slope suggests a mild departure from the ΛCDM paradigm pointing to a quintessence-like dark energy behavior with a slowly evolving equation of state.

8 Model selection and information criteria and model selection

Model selection is the process of identifying the most appropriate candidate among various models with different numbers of free parameters. The least-squares (χ^2) method is commonly used in cosmology for comparing model fits, but it does not account for differences in degrees of freedom. When comparing models with different numbers of parameters, a model with more free parameters may have a lower χ^2 simply due to its flexibility, rather than its true explanatory power.

To address this we compute the reduced chi-squared statistic, defined as [60]

$$\chi^2_{\rm red} = \frac{\chi^2}{N - K}, \tag{62}$$

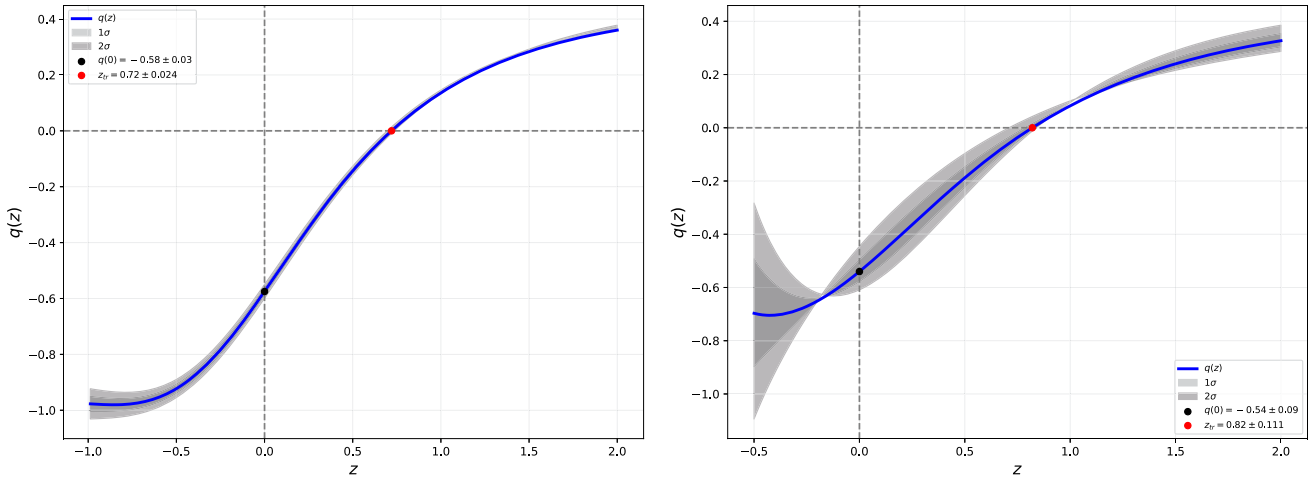

(a) Model-1 **(b)** Model-2

Fig. 7 Redshift evolution of the deceleration parameter $q(z)$ for Model-1 (left) and Model-2 (right), illustrating the transition from cosmic deceleration to acceleration

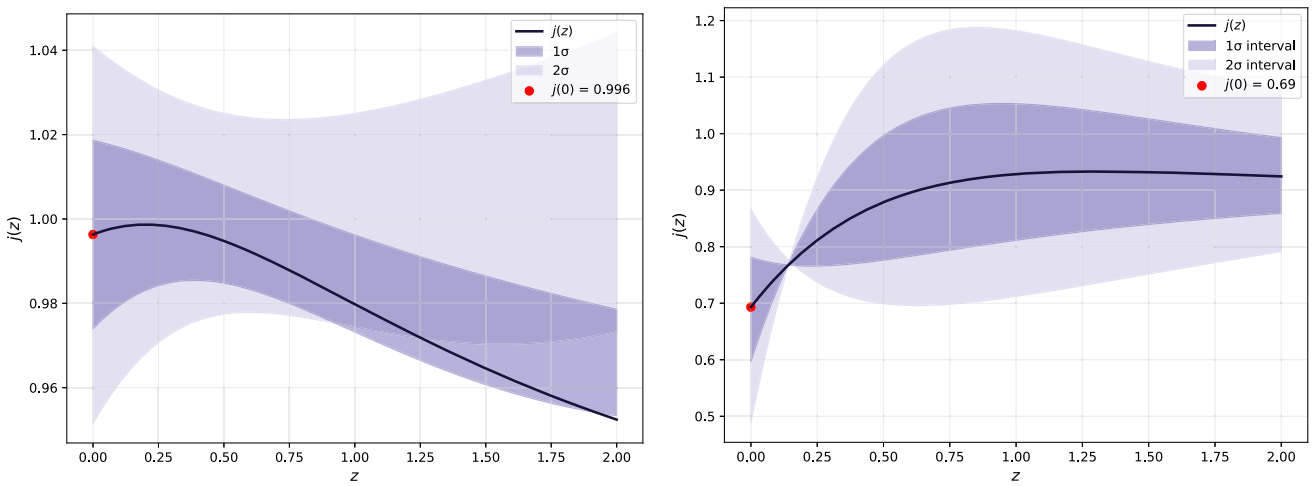

(a) Model-1 **(b)** Model-2

Fig. 8 Redshift evolution of the jerk parameter $j(z)$ for Model-1 (left) and Model-2 (right), providing insights into the dynamics of cosmic acceleration beyond the deceleration phase

where N is the total number of data points and K is the number of free parameters. A value of $\chi^2_{\rm red} \approx 1$ indicates a good fit, $\chi^2_{\rm red} \gg 1$ indicates a poor fit, and $\chi^2_{\rm red} \ll 1$ may signal overfitting or overestimated errors. The results for $\chi^2_{\rm red}$ are shown in Table 3. The reduced chi-squared values for all models ($\chi^2_{\rm red} \approx 0.64 - 0.84$) are less than unity, indicating that the models fit the observational data well and that the quoted uncertainties may be slightly conservative.

To assess and compare the statistical performance of our cosmological models, we employ standard model selection tools rooted in information theory. Specifically, we utilize the Akaike information criterion (AIC) [61] and the Bayesian information criterion (BIC) [62] to quantitatively evaluate model adequacy and relative likelihood.

The AIC is designed to estimate the relative quality of statistical models for a given dataset balancing the trade-off between model complexity and goodness-of-fit. For models assuming Gaussian errors, the AIC is calculated as [63]

$$\mathrm{AIC} = -2\ln\mathcal{L}_{\rm max} + 2k + \frac{2k(k+1)}{N_{\rm tot} - k - 1}, \tag{63}$$

where k denotes the number of model parameters, $\mathcal{L}_{\rm max}$ is the maximum likelihood obtained from the fit and $N_{\rm tot}$ is the total number of data points. In the limit of large data samples, the

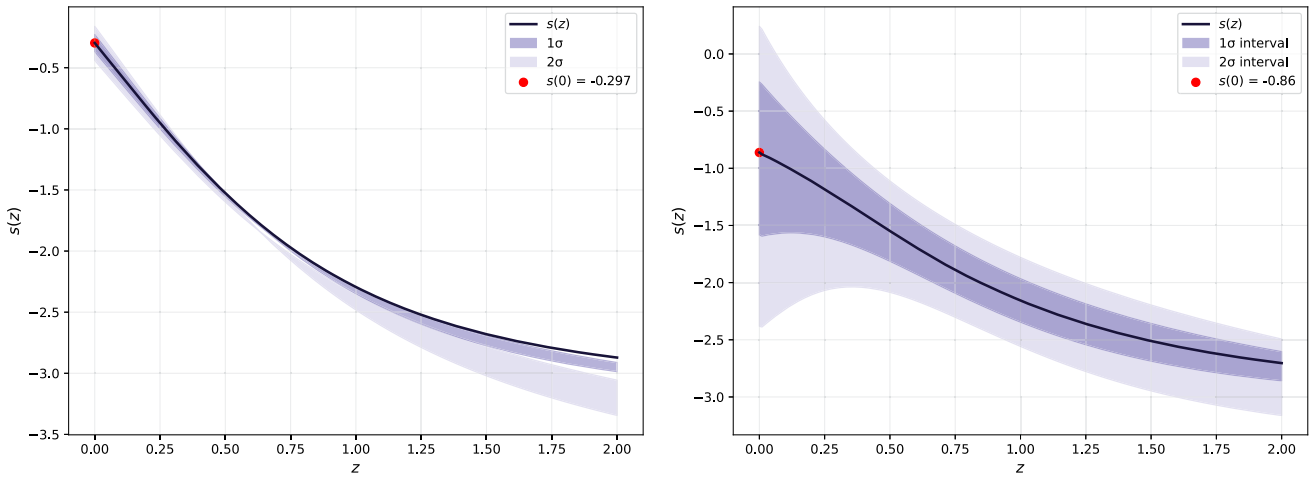

(a) Model-1 **(b)** Model-2

Fig. 9 Redshift evolution of the snap parameter $s(z)$ for Model-1 (left) and Model-2 (right), capturing higher-order deviations in the expansion history and offering complementary insights into the dynamics of dark energy

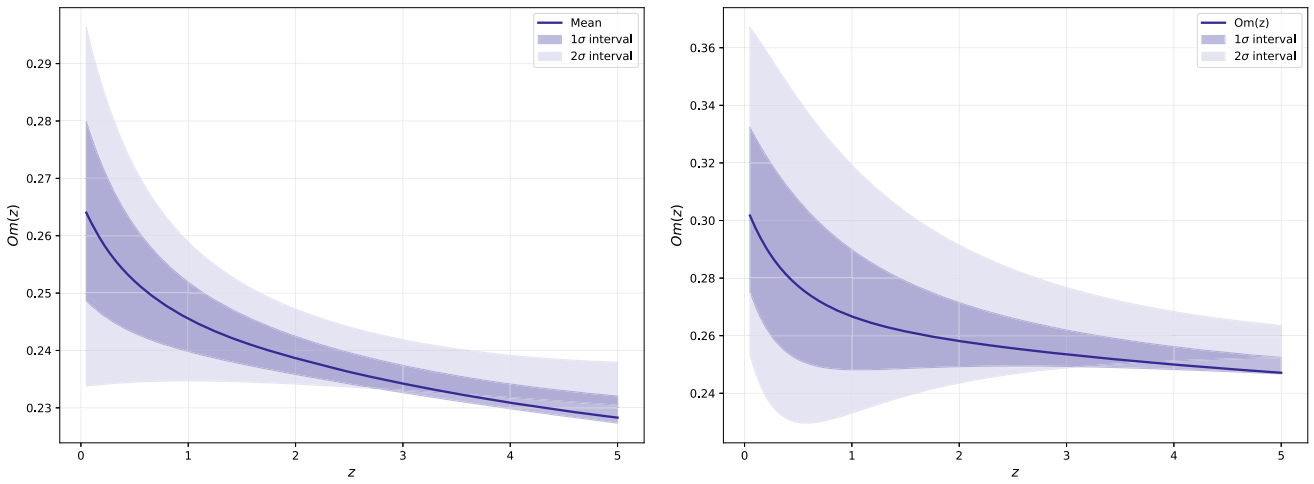

(a) Model-1 **(b)** Model-2

Fig. 10 Redshift evolution of the $Om(z)$ diagnostic for Model-1 (left) and Model-2 (right), used to assess deviations from the standard ΛCDM model

correction term becomes negligible, yielding the commonly used form AIC $\approx -2\ln\mathcal{L}_{\max} + 2k$.

The BIC on the other hand is based on Bayesian inference and incorporates a more substantial penalty for model complexity, given by

$$\mathrm{BIC} = -2\ln\mathcal{L}_{\max} + k\ln N_{\mathrm{tot}}, \tag{64}$$

penalizing additional parameters more strongly as the dataset grows.

For model comparison we compute the difference between each model information criterion (IC) value and the minimum value across all considered models [57,63]

$$\Delta\mathrm{IC}_{\mathrm{model}} = \mathrm{IC}_{\mathrm{model}} - \mathrm{IC}_{\mathrm{min}}, \tag{65}$$

where $\mathrm{IC}_{\mathrm{min}}$ represents the best-performing model according to the chosen criterion. This ΔIC provides a direct measure of how well each model performs relative to the best candidate.

Interpretation of these values is guided by standard thresholds [58]: models with $\Delta\mathrm{IC} \leq 2$ are considered statistically indistinguishable from the best-fit model; $2 < \Delta\mathrm{IC} < 6$ suggests moderate evidence against a model; and $\Delta\mathrm{IC} \geq 10$ indicates strong disfavor by the data. Table 3 shows that for both datasets, Model-1 attains a slightly lower χ^2_{min} than ΛCDM, indicating a marginally better fit, while Model-2 yields comparatively higher χ^2_{min} values.

For the CC+BAO dataset, Model-1 remains close to ΛCDM in performance according to AIC ($\Delta AIC = 2.55 < 4$),

while BIC gives a larger separation ($\Delta BIC = 6.64 > 6$). Model-2 exhibits higher AIC and BIC differences ($\Delta AIC = 12.47$, $\Delta BIC = 12.90$) for this dataset. For the joint CC+BAO+SNIe dataset, AIC shows Model-1 to be nearly equivalent to ΛCDM ($\Delta AIC = 1.44 < 2$), while BIC again reports a larger numerical gap ($\Delta BIC = 12.39$). Model-2 shows higher AIC and BIC differences in this case as well ($\Delta AIC = 9.83$, $\Delta BIC = 15.67$).

9 Summary of the work and future perspectives

The current study employs Finsler–Barthel–Kropina spacetime geometry to examine cosmic evolution and dark energy behavior by incorporating observational data sets-including cosmic chronometers (CC), baryon acoustic oscillations (BAO) and type Ia supernovae (SNe Ia). The approach within Finsler geometry provides a framework for investigating cosmological dynamics, notably its ability to model anisotropic effects in the expansion of the universe. By exploiting the adaptability of the Kropina-type metric in conjunction with the Barthel connection, the model effectively captures the intricate interplay between dark energy and cosmic expansion yielding results that are consistent with observational data over different parameters. Moreover the we discuss cosmological models that inherently incorporate direction-dependent metrics, thereby establishing a generalized Kropina-type space capable of representing anisotropic expansion dynamics. In this framework the combination of a Riemannian metric with an additional one-form serves as an effective tool for modeling anisotropic cosmic expansion offering a versatile method to interpret cosmic acceleration through parameterizations that are directly responsive to cosmological observations.

Further, we implement a linear parametrization for the anisotropy parameter $\eta(z)$ enabling a direct investigation of anisotropic effects within the Finsler–Barthel–Kropina cosmological framework. Two representative dark energy models are systematically examined: (i) Model-1, characterized by a constant equation-of-state parameter $\omega_{\rm de}$, and (ii) Model-2, which employs a redshift-dependent CPL form, $\omega_{\rm de}(z) = \omega_0 + \omega_1 \frac{z}{1+z}$ allowing for dynamical evolution of dark energy. The constant-ω scenario of Model-1 demonstrates close alignment with the standard ΛCDM model reinforcing the validity of a temporally invariant dark energy component under current data. Conversely, Model-2 provides a more general and adaptable framework, capturing possible late-time departures from cosmic isotropy and accommodating a time-varying dark energy equation of state.

The empirical analysis of the anisotropy parameter n reveals a marked sensitivity to dataset composition, underscoring the model's potential to probe and constrain deviations from isotropy. Both models yield Hubble constant estimates, $H_0 = 69.47 \pm 0.44$ (Model-1) and $H_0 = 70.86 \pm 0.32$ (Model-2), values that lie between the lower Planck CMB and higher SH0ES determinations, thereby partially alleviating the H_0 tension. Notably, Model-2 demonstrates enhanced sensitivity to the inclusion of BAO and SNe Ia data, which translates to a more refined description of evolving cosmic acceleration. A comprehensive assessment of the energy conditions establishes the physical viability of both models: the null, weak, and dominant energy conditions are preserved across the observationally relevant epoch, while the temporary violation of the strong energy condition in both Model-1 and Model-2 at low redshifts directly correlates with the observed transition to cosmic acceleration. This signature is further supported by the evolution of cosmographic diagnostics such as $q(z)$, $j(z)$, and $s(z)$-and the $Om(z)$ function, which collectively demonstrate the models ability to encapsulate non-trivial dynamical features and provide a quantitative framework for testing anisotropic cosmological scenarios.

The results presented here have significant implications for both theory and observation. The Finsler–Barthel–Kropina framework emerges as a compelling extension of standard cosmology, offering new avenues to characterize and constrain cosmic anisotropy using current and future observational datasets. In particular, the evidence for late-time anisotropy and dynamic dark energy within this geometric context not only enriches our understanding of cosmic acceleration but also opens the possibility of distinguishing between fundamentally different gravitational and dark energy paradigms. This work thus lays the groundwork for a broader program of confronting Finslerian and other generalized geometric models with precision cosmological data, aiming to uncover subtle signatures of new physics beyond ΛCDM.

The novelty of our work lies in the formulation of a Barthel–Kropina Finslerian framework that not only accommodates anisotropic cosmological scenarios but also presents a mathematically robust extension compatible with observational data. This approach deepens our understanding of how cosmic anisotropies and inhomogeneities influence large-scale dynamics, offering a compelling direction for future observational and theoretical investigations in cosmology.

Future perspectives

As anticipated, the findings presented herein pave the way for exploring a broad spectrum of related cosmological phenomena. In closing, we outline several pertinent directions that merit attention in future studies:

- The scope for future research could extend the Barthel–Kropina Finsler framework by incorporating higher-order corrections and exploring alternative Finslerian spaces or connections, such as Berwald or Cartan connections, to enhance the versatility of cosmological models.

Table 3 Model selection statistics and information criteria for Model-1, Model-2, and ΛCDM, using both CC+BAO and joint (CC+BAO+SNIe) datasets

Dataset	Model	χ^2_{min}	χ^2_{red}	AIC	BIC	ΔAIC	ΔBIC
CC+BAO	ΛCDM	33.45	0.62	39.45	45.58	0	0
	Model-1	32.00	0.62	42.00	52.22	2.55	6.64
	Model-2	39.92	0.74	51.92	58.48	12.47	12.90
Joint	ΛCDM	1447.04	0.83	1455.04	1476.93	0	0
	Model-1	1444.49	0.82	1456.49	1489.32	1.44	12.39
	Model-2	1452.87	0.83	1464.87	1492.60	9.83	15.67

The inclusion of additional observational datasets can refine parameter constraints and validate the anisotropic models more rigorously. This work lays the groundwork for a broader application of anisotropic models in cosmology, providing a foundation for addressing unresolved questions about dark energy, cosmic anisotropies, and deviations from the standard Λ-CDM paradigm.

- The Barthel–Kropina model also supports the exploration of early universe physics, particularly in inflationary models and scalar field dynamics, where anisotropies may have impacted primordial perturbations. Its adaptability allows for the study of modified gravity theories, potentially illuminating deviations from general relativity and aiding in the understanding of dark energy's nature.
- Gravitational wave (GW): This theoretical approach could be adapted to investigate GW propagation, offering insights into wave dispersion and polarization in anisotropic space-time that could be detected with next-generation observatories.
- Gravitational lensing: This framework could enhance predictions of cosmic shear and weak gravitational lensing patterns, refining our models for lensing in the presence of directional dependencies.
- The model anisotropic characteristics may help explain certain anomalies observed in the cosmic microwave background (CMB), such as hemispherical asymmetry and multipole alignments, that remain challenging to address within standard isotropic frameworks.

Acknowledgements The first author JP, thanks the University of Grant Commission, India, for financial support via UGC-Junior Research Fellowship (Student ID-231610191052) / (Dec-2022 / June-2023-CSIR-UGC NET). Author RK is thankful to IUCCA, Pune, India, for providing facilities under associateship programs where a part of the work is done during his visit. The authors also express their sincere gratitude to the anonymous reviewer for their valuable suggestions, which significantly improved the quality and presentation of the research.

Funding No funding was received for this research.

Data Availability Statement This manuscript has no associated data. [Author's comment: This manuscript has no associated data.]

Code Availability Statement This manuscript has no associated code/software. [Author's comment: This manuscript has no associated code/software.]

Declarations

Conflict of interest The authors confirm that there are no financial interests or personal affiliations that could have influenced the research presented in this paper.

Funded by SCOAP[3].

References

1. A.G. Riess, A.V. Filippenko, P. Challis, A. Clocchiatti, A. Diercks, P.M. Garnavich, J. Tonry, Observational evidence from supernovae for an accelerating universe and a cosmological constant. Astron. J. **116**(3), 1009 (1998)
2. S. Perlmutter, B.P. Schmidt, Measuring cosmology with supernovae, in *Supernovae and Gamma-Ray Bursters* (pp. 195–217) (2003)
3. S. Perlmutter, Supernovae, dark energy, and the accelerating universe. Phys. Today **56**(4), 53–60 (2003)
4. J.L. Tonry, B.P. Schmidt, B. Barris, P. Candia, P. Challis, A. Clocchiatti, N.B. Suntzeff, Cosmological results from high-z supernovae. Astrophys. J. **594**(1), 1 (2003)
5. B.P. Schmidt, N.B. Suntzeff, M.M. Phillips, R.A. Schommer, A. Clocchiatti, R.P. Kirshner, R. Ciardullo, The high-z supernova search: measuring cosmic deceleration and global curvature of the universe using type ia supernovae. Astrophys. J. **507**(1), 46 (1998)
6. L. Amendola, S. Tsujikawa, *Dark Energy: Theory and Observations* (Cambridge University Press, Cambridge, 2010)
7. E. Komatsu, A. Kogut, M.R. Nolta, C.L. Bennett, M. Halpern, G. Hinshaw, E.L. Wright, First-year wilkinson microwave anisotropy

probe (wmap)* observations: tests of gaussianity. Astrophys. J. Suppl. Ser. **148**(1), 119 (2003)
8. D.N. Spergel, L. Verde, H.V. Peiris, E. Komatsu, M.R. Nolta, C.L. Bennett, E.L. Wright, First-year wilkinson microwave anisotropy probe (wmap)* observations: determination of cosmological parameters. Astrophys. J. Suppl. Ser. **148**(1), 175 (2003)
9. D.J. Eisenstein, I. Zehavi, D.W. Hogg, R. Scoccimarro, M.R. Blanton, R.C. Nichol, D.G. York, Detection of the baryon acoustic peak in the large-scale correlation function of sdss luminous red galaxies. Astrophys. J. **633**(2), 560 (2005)
10. S.F. Daniel, R.R. Caldwell, A. Cooray, A. Melchiorri, Large scale structure as a probe of gravitational slip. Phys. Rev. D Part. Fields Gravit. Cosmol. **77**(10), 103513 (2008)
11. V. Sahni, A. Starobinsky, The case for a positive cosmological λ-term. Int. J. Mod. Phys. D **9**(04), 373–443 (2000)
12. T. Padmanabhan, Cosmological constant-the weight of the vacuum. Phys. Rep. **380**(5–6), 235–320 (2003)
13. R.R. Caldwell, A phantom menace? cosmological consequences of a dark energy component with super-negative equation of state. Phys. Lett. B **545**(1–2), 23–29 (2002)
14. S.M. Carroll, M. Hoffman, M. Trodden, Can the dark energy equation-of-state parameter ω be less than -1. Phys. Rev. D **68**(2), 023509 (2003)
15. J.A.S. Lima, J.V. Cunha, J.S. Alcaniz, Constraining the dark energy with galaxy cluster x-ray data. Phys. Rev. D **68**(2), 023510 (2003)
16. J. Weller, A. Albrecht, Opportunities for future supernova studies of cosmic acceleration. Phys. Rev. Lett. **86**(10), 1939 (2001)
17. E.V. Linder, Exploring the expansion history of the universe. Phys. Rev. Lett. **90**(9), 091301 (2003)
18. E.M. Barboza Jr., J.S. Alcaniz, A parametric model for dark energy. Phys. Lett. B **666**(5), 415–419 (2008)
19. P.C. Stavrinos, On the generalized metric structure of space-time: finslerian anisotropic gravitational field. J. Phys. Conf. Ser. **8**(1), 49 (2005)
20. S.F. Rutz, A finsler generalisation of Einstein's vacuum field equations. Gen. Relativ. Gravit. **25**, 1139–1158 (1993)
21. Yu.G. Bogoslovsky, A viable model of locally anisotropic space-time and the finslerian generalization of the relativity theory. Fortschritte der Physik/Progress of Physics **42**(2), 143–193 (1994)
22. G.Y. Bogoslovsky, H.F. Goenner, Finslerian spaces possessing local relativistic symmetry. Gen. Relativ. Gravit. **31**(10), 1565–1603 (1999)
23. S.I. Vacaru, Superstrings in higher order extensions of finsler superspaces. Nucl. Phys. B **494**(3), 590–656 (1997)
24. S.I. Vacaru, Spinors and field interactions in higher order anisotropic spaces. J. High Energy Phys. **1998**(09), 011 (1998)
25. P.C. Stavrinos, A.P. Kouretsis, M. Stathakopoulos, Friedman-like Robertson–Walker model in generalized metric space-time with weak anisotropy. Gen. Relativ. Gravit. **40**, 1403–1425 (2008)
26. P. Stavrinos, Gravitational and cosmological considerations based on the finsler and lagrange metric structures. Nonlinear Anal. Theory Methods Appl. **71**(12), e1380–e1392 (2009)
27. D.G. Pavlov, Could kinematical effects in the cmb prove finsler character of the space-time? AIP Conf. Proc. **1283**(1), 180–186 (2010)
28. A.P. Kouretsis, M. Stathakopoulos, P.C. Stavrinos, General very special relativity in finsler cosmology. Phys. Rev. D Part. Fields Gravit. Cosmol. **79**(10), 104011 (2009)
29. G.W. Gibbons, J. Gomis, C.N. Pope, General very special relativity is finsler geometry. Phys. Rev. D Part. Fields Gravit. Cosmol. **76**(8), 081701 (2007)
30. V. Balan, G.Y. Bogoslovsky, S.S. Kokarev, D.G. Pavlov, S.V. Siparov, N. Voicu, Geometrical models of the locally anisotropic space-time (2011). arXiv:1111.4346
31. I.P. Lobo, N. Loret, F. Nettel, Investigation of finsler geometry as a generalization to curved space-time of Planck-scale-deformed relativity in the de sitter case. Phys. Rev. D **95**(4), 046015 (2017)
32. S.I. Vacaru, Principles of einstein-finsler gravity and perspectives in modern cosmology. Int. J. Mod. Phys. D **21**(09), 1250072 (2012)
33. Z. Chang, S. Wang, X. Li, Fine structure constant variation or space-time anisotropy? Eur. Phys. J. C **72**, 1–6 (2012)
34. S. Basilakos, P. Stavrinos, Cosmological equivalence between the finsler-randers space-time and the dgp gravity model. Phys. Rev. D Part. Fields Gravit. Cosmol. **87**(4), 043506 (2013)
35. A. Triantafyllopoulos, S. Basilakos, E. Kapsabelis, P.C. Stavrinos, Schwarzschild-like solutions in finsler-randers gravity. Eur. Phys. J. C **80**(12), 1200 (2020)
36. M. Hohmann, C. Pfeifer, N. Voicu, Cosmological Finsler spacetimes. Universe **6**(5), 65 (2020)
37. R. Raushan, R. Chaubey, Finsler-randers cosmology in the framework of a particle creation mechanism: a dynamical systems perspective. Eur. Phys. J. Plus **135**(2), 228 (2020)
38. S. Ikeda, E.N. Saridakis, P.C. Stavrinos, A. Triantafyllopoulos, Cosmology of lorentz fiber-bundle induced scalar-tensor theories. Phys. Rev. D **100**(12), 124035 (2019)
39. J.E.G. Silva, A field theory in randers-finsler space-time. Europhys. Lett. **133**(2), 21002 (2021)
40. R. Hama, T. Harko, S.V. Sabau, Dark energy and accelerating cosmological evolution from osculating barthel-kropina geometry. Eur. Phys. J. C **82**(4), 1–25 (2022)
41. A. Bouali, H. Chaudhary, R. Hama, T. Harko, S.V. Sabau, M.S. Martín, Cosmological tests of the osculating barthel-kropina dark energy model. Eur. Phys. J. C **83**(2), 121 (2023)
42. S.K. Narasimhamurthy, J. Praveen, Cosmological constant roll of inflation within finsler-barthel-kropina geometry: a geometric approach to early universe dynamics. New Astron. **108**, 102187 (2024)
43. J. Praveen, S.K. Narasimhamurthy, Investigating late-time cosmology using finsler-randers geometry and barthel connection: observational constraints and implications. Nucl. Phys. B 116899 (2025)
44. G.S. Asanov, *Finsler Geometry, Relativity and Gauge Theories*, vol. 12 (Springer Science and Business Media, 2012)
45. C. Pfeifer, Finsler space-time geometry in physics. Int. J. Geom. Methods Mod. Phys. **16**(supp02), 1941004 (2019)
46. H. Rund, *The Differential Geometry of Finsler Spaces*, vol. 101. (Springer Science and Business Media, 2012)
47. M. Matsumoto, Theory of finsler spaces with α, β-metric. Rep. Math. Phys. **31**(1), 43–83 (1992)
48. R.S. Ingarden, Vector field relative finsler space in two physical examples. Nonlinear World **4**, 85–100 (1997)
49. R.S. Ingarden, L. Tamássy, The point finsler spaces and their physical applications in electron optics and thermodynamics. Math. Comput. Model. **20**(4–5), 93–107 (1994)
50. R.S. Ingarden, M. Matsumoto, On the 1953 barthel connection of a finsler space and its mathematical and physical interpretation. Rep. Math. Phys. **32**(1), 35–48 (1993)
51. M. Koussour, N. Myrzakulov, M.K.M. Ali, Exploring universe acceleration through observational constraints via hubble parameter reconstruction. J. High Energy Astrophys. **42**, 96–103 (2024)
52. S.A. Narawade, B. Mishra, Phantom cosmological model with observational constraints in $f(q)$ gravity. Ann. Phys. **535**(5), 2200626 (2023)
53. D. Wang, M. Koussour, A. Malik, N. Myrzakulov, G. Mustafa, Observational constraints on a logarithmic scalar field dark energy model and black hole mass evolution in the universe. Eur. Phys. J. C **83**(7), 1–14 (2023)
54. S.K.J. Pacif, Dark energy models from a parametrization of h: a comprehensive analysis and observational constraints. Eur. Phys. J. Plus **135**(10), 1–34 (2020)

55. R.C. Bernardo, D. Grandón, J.L. Said, V.H. Cárdenas, Parametric and nonparametric methods hint dark energy evolution. Phys. Dark Univ. **36**, 101017 (2022)
56. R.C. Bernardo, D. Grandón, J.L. Said, V.H. Cárdenas, Dark energy by natural evolution: constraining dark energy using approximate Bayesian computation. Phys. Dark Univ. **40**, 101213 (2023)
57. A.E. Raftery, Approximate bayes factors and accounting for model uncertainty in generalised linear models. Biometrika **83**(2), 251–266 (1996)
58. K.P. Burnham, D.R. Anderson, Multimodel inference: understanding aic and bic in model selection. Sociol. Methods Res. **33**(2), 261–304 (2004)
59. A.G. Riess, W. Yuan, L.M. Macri, D. Scolnic, D. Brout, S. Casertano et al., A comprehensive measurement of the local value of the hubble constant with 1 km s^{-1} mpc^{-1} uncertainty from the hubble space telescope and the sh0es team. Astrophys. J. Lett. **934**(1), L7 (2022)
60. P.R. Bevington, D.K. Robinson, *Data Reduction and Error Analysis* (McGraw-Hill, New York, 2003)
61. H. Akaike, A new look at the statistical model identification. IEEE Trans. Autom. Control **19**(6), 716–723 (2003)
62. G. Schwarz, Estimating the dimension of a model. Ann. Stat. 461–464 (1978)
63. D.J. Spiegelhalter, N.G. Best, B.P. Carlin, A. Linde, Bayesian measures of model complexity and fit. J. R. Stat. Soc. Ser. B (statistical Methodology) **64**(4), 583–639 (2002)